Engineered Mesenchymal Stem Cells Targeting P2X7 Receptor for Immunomodulation in Traumatic Brain Injury

Lucia Fadon Padilla[1] PhD, Chinmoy Sarkar[2] PhD, Marta Lipinski[2] PhD, Shalini Sharma[1] PhD, Chengyan Chu[1] MD, Miroslaw Janowski[1] MD, PhD, Piotr Walczak[1] MD, PhD

[1]Department of Diagnostic Radiology and Nuclear Medicine, University of Maryland School of Medicine, Baltimore, MD. [2]Department of Anesthesiology University of Maryland School of Medicine, Baltimore, MD.

Background: Traumatic brain injury (TBI) is a leading cause of long-term disability, with inflammation playing a key role in both the primary and secondary phases of brain damage. Among the molecular triggers, extracellular ATP and its receptor P2X7 are potent drivers of neuroinflammation and represent promising therapeutic targets.

Objective: We aim to develop a novel therapeutic strategy to mitigate acute inflammation after TBI by employing engineered cells that deliver a P2X7-blocking nanobody. Our initial tests were with glial progenitor cells (GRPs); however, only small fraction of these small size progenitors home to the brain after intra-arterial administration. Here we aim to explore whether mesenchymal stem cells (MSCs) result in robust brain engraftment.

Methods: *In vitro*, primary MSCs were transfected with bicistronic mRNA encoding a HaloTag reporter and a nanobody targeting P2X7. Transfection efficiency was assessed via flow cytometry. *In vivo*, closed head injury (CHI) was induced in mice. 24 hours post-TBI, for MRI tracking P2X7-expressing MSCs were labeled with iron oxide nanoparticles (Molday) and were administered via intra-arterial injection. Mice with catheters placed for selective targeting of internal carotid artery were positioned in 9.4T MRI scanner for dynamic imaging. Cellular accumulation in the brain was evaluated dynamically using susceptibility-weighted imaging (SWI) MRI as hypointense signal. Behavioral performance was assessed using the beam walk test, and mice were sacrificed at day 4 post-TBI for immunofluorescence analysis of cell localization.

Results: mRNA transfection resulted in a transfection efficiency of approximately 40% (**Fig.1A**). SWI MRI revealed accumulation of labeled MSCs in the brain post-injection, with signal detectable up to 3 days (**Fig.1B–E**). Behavioral testing indicated no motor or cognitive impairment due to MSC administration (**Fig.1F**). Immunofluorescence confirmed the presence of transfected cells in the injured brain tissue (**Fig.1G–H**).

Conclusions: We demonstrate that engineered MSCs expressing a P2X7-blocking nanobody successfully engraft in the injured brain tissue and remain detectable up to 3 days post-injection. No adverse effects were observed in behavioral assessments, supporting the safety of this approach. These findings establish a foundation for exploring cell-based immunomodulatory therapies targeting neuroinflammation in TBI. Additionally, our work highlights the value of non-invasive *in vivo* imaging techniques such as MRI to monitor the biodistribution and persistence of therapeutic cells.
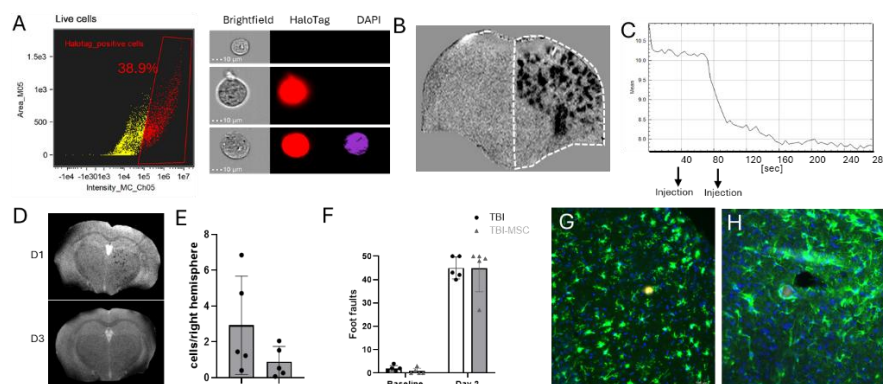
(A) Flow cytometry dot plot of primary GRPs 24 hours after transfection with P2X7 mRNA, and representative fluorescence image showing HaloTag expression in a transfected cell.(B) MRI SWI image generated by subtracting pre- and post-injection scans, showing hypointense signal corresponding to Molday-labeled MSCs accumulating in the right hemisphere following intra-arterial injection.(C) Quantification of hypointense signal over 280 seconds in the right hemisphere, during which two pulses of MSCs were injected. (D) Representative SWI images showing cell accumulation immediately after intra-arterial injection (D1) and day 3 post-injection (D3). (E) Quantification of hypointense signal in the right hemisphere on SWI images.(F) Beam walk test results showing foot faults per 50 steps at baseline and 2 days post-TBI. (G-H) Immunofluorescence images of HaloTag-labeled GRPs co-stained with IBA1 or GFAP.

Radiolabeling of human mesenchymal stem cells for intra-arterial brain delivery to treat stroke

Sharma S, Gulisashvili D, Salemdawod A, Kalkowski L, Brzezinski M, Liang Y, Walczak, P, Janowski M
Program in Image Guided Neurointerventions, Center for Advanced Imaging Research. Department of Diagnostic Radiology and Nuclear Medicine, University of Maryland, Baltimore.

Background: Mesenchymal stem cells (MSCs) are highly promising therapeutic agents. However, unknown biodistribution upon transplantation limits the understanding of their therapeutic effects. This limitation particularly affects advanced and more precise intra-arterial routes of cell delivery.

Objective: To develop and optimize the radiolabeling of MSCs to facilitate image-guided precision medicine.

Methods: The radiolabeling procedure involves chelating ^{89}Zr atoms with deferoxamine (DFO), which is then incubated with cells for 30 minutes in Eppendorf tubes. After washing, the cells are analyzed for radioactivity uptake, cell survival, and cell proliferation and metabolism as measured by CCK8 assay over a week (days 1,3, 5, 7). We used 100k MSCs per sample throughout the study, as it is a typical dose for intra-arterial delivery to the brain. Independent variables include cell concentration (10k/mL and 2k/mL), added radioactivity per sample, and radiation intensity during incubation. Radioactivity captured per cell uniquely serves as both types of variables depending on the situation. Dependent variables include radioactivity captured per cell (labeling yield), labeling efficiency, radioactivity efflux after a day and a week, cell viability, and cell proliferation and metabolism. We conducted four repetitions of the experiment, totaling 1464 data points.

Results: We observed that lower cell concentration (2k/mL) was associated with better outputs across all dependent variables. However, the condition characterized by the highest uptake radioactivity per cell and the most favorable CCK8 assay included higher cell concentration (10k/mL) **(Fig. 1a)**. As expected, adding more radioactivity and achieving higher radiation intensity allowed for better radioactivity yield per cell **(Fig. 1b)**, which led to a higher efflux of radioactivity afterward **(Fig. 1c)**. While higher radioactivity uptake per cell decreased the cell viability at the end of the radiolabeling procedure **(Fig. 1d)**, it positively affected MSC proliferation and metabolism **(Fig. 1e,f)**.

Conclusions: We have shown that lower cell concentration resulted in positive effects across all dependent variables. Higher radioactivity per cell also contributed to better cell proliferation and metabolism, obviating negative long-term consequences of radioactivity on cell well-being, even if it negatively affected cell survival during the procedure. Interestingly, we have observed accelerated growth of MSCs with high radioactivity per cell, which requires further investigation.
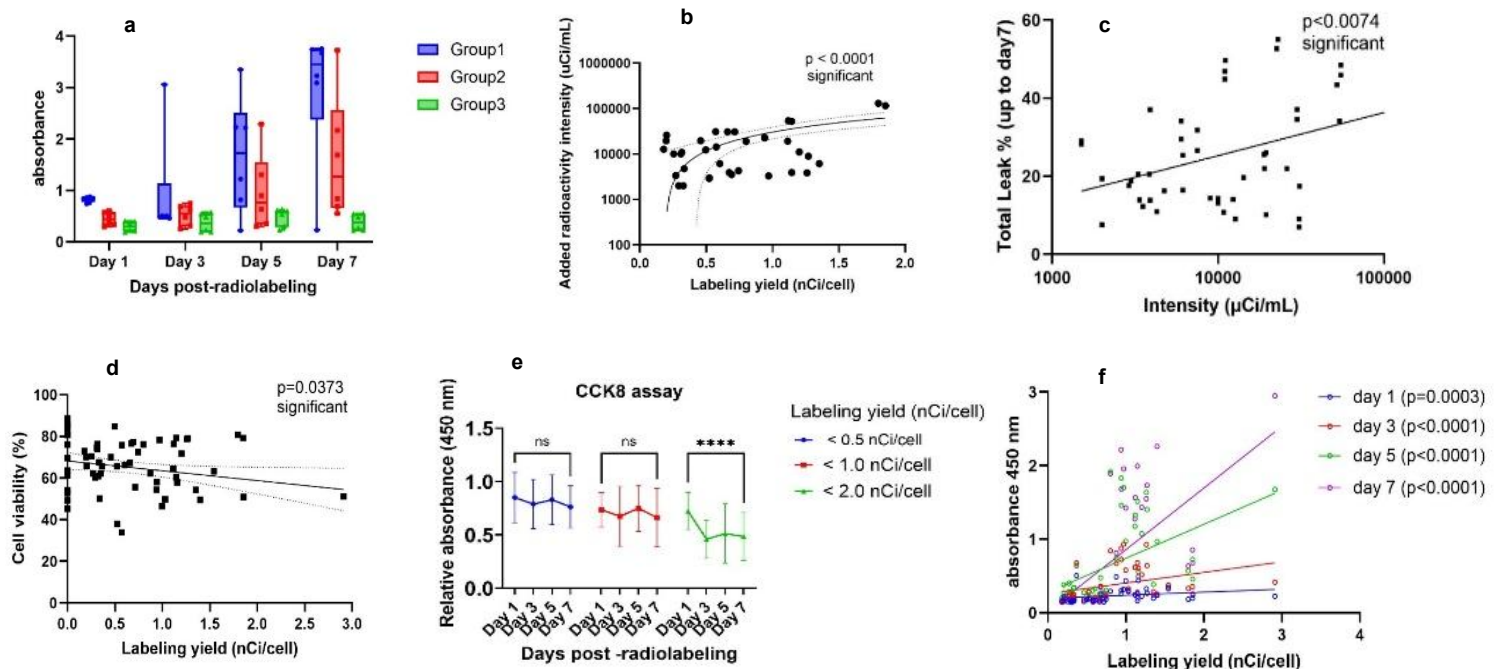

Figure 1. Mesenchymal stem cell radiolabeling analysis

CellposeCellCounter: A Web-Based AI-Driven Platform for Automated Cell Counting and Viability Assessment

Matthew Yang[1], Laasya Ravipati[1], Fengtong Du[2], Yajie Liang PhD[1], Miroslaw Janowski PhD[1]

[1]Department of Diagnostic Radiology and Nuclear Medicine, University of Maryland School of Medicine, Baltimore, MD, USA; [2]Janelia Research Campus, Ashburn, VA, USA

Background: Accurate and low-cost quantification of cells is vital for assessing cell viability and proliferation in biomedical research. Current methods of quantification such as hemocytometer counting are labor-intensive and prone to error. On the other hand, automated cell counting based on microscope images or flow cytometry are fast but require expensive hardware. With the onset of modern AI segmentation models such as Cellpose-SAM[1], the task of cell counting can be automated and easily accessible[2].
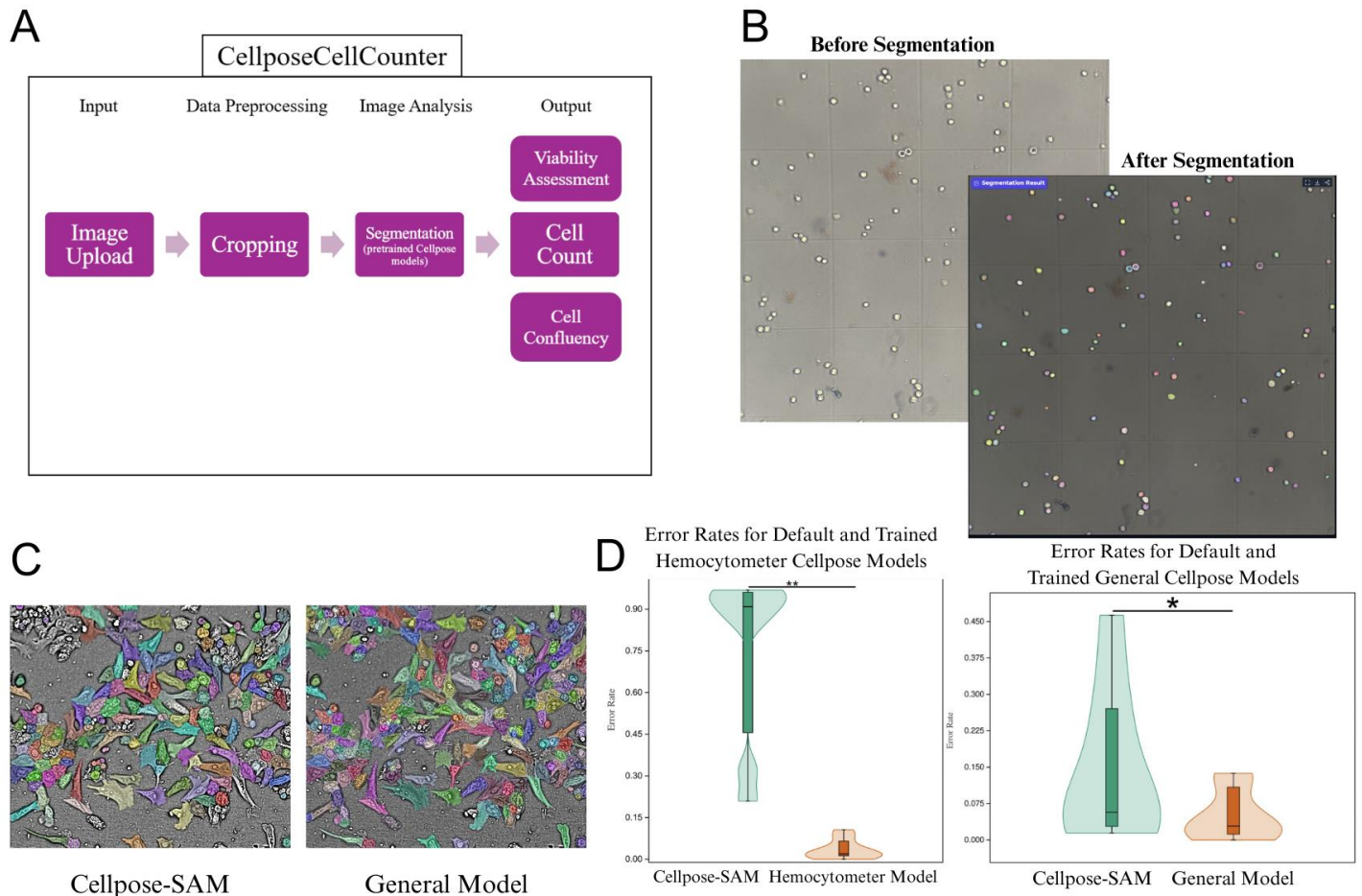
Objective: To develop web-based platform for automatic, accurate, and free cell counting, confluency measurement, and viability assessment, and to evaluate its performance in comparison to traditional manual cell counting tools such as hemocytometers.

Methods: We created *CellposeCellCounter*, a GPU-accelerated web application on Hugging Face Spaces (**Figure 1A**). The application utilizes Cellpose-SAM, a generalist segmentation algorithm, to segment cells. To improve accuracy, we trained two custom models using the default Cellpose-SAM model available in the Cellpose GUI, for suspended cells in hemocytometer (Hemocytometer Model) and adherent cells in culture (General Model). Models were trained through iterative correction of output segmentations by users (Human-in-the-loop ML). The models were deployed to *CellposeCellCounter* on a publicly accessible Hugging Face Space. The interface allowed users to upload images and define regions of interest (ROIs) through cropping, freehand drawing, or manual coordinate input. A thresholding tool was implemented to assess cell viability based on pixel color and intensity values associated with Trypan Blue uptake. Users set threshold parameters using a slider interface to select for stained (dead) cells. To use the app, images are first uploaded, and then users select the desired model for segmentation. The application then performed segmentation within the selected ROI and returned outputs including live cell count, dead cell count, cell confluency, viability percentage, and the original image overlaid with the predicted segmentation masks, color-coded based on viability (**Figure 1B**).

Results: Model training resulted in significantly lower segmentation errors compared to the default model (**Figure 1C**). Error rates were gathered from a test dataset for both the Hemocytometer Model and General Model in comparison with the default Cellpose-SAM model, as shown in **Figure 1D**. P-values of 0.0078 and 0.0156 were obtained from Wilcoxon Signed-Rank Tests comparing the error rates of the Hemocytometer Model and the General Model against the default model, respectively. Inference times for *CellposeCellCounter* reached no more than 15 seconds, even on larger images (1024x1024), on-par with traditional automated cell counters.

Conclusions: The findings demonstrate *CellposeCellCounter*'s utility as a convenient tool for accurate automated cell counting and viability assessment across a wide variety of images, establishing it as a freely available alternative to traditional cell counting methods.

References: 1. Pachitariu M, Rariden M, Stringer C. Cellpose-SAM: superhuman generalization for cellular segmentation. bioRxiv. Published May 1, 2025. doi:10.1101/2025.04.28.651001 2. Hernández CX, Sultan MM, Pande VS. Using deep learning for segmentation and counting within microscopy data. arXiv. Published February 28, 2018. Accessed July 31, 2025. https://arxiv.org/abs/1802.10548

Figure 1. Overview and performance of the *CellposeCellCounter* web application. **(A)** Example workflow in *CellposeCellCounter* **(B)** Comparison between the input image prior to segmentation and produced output after segmentation. Colored masks indicate segmentations. **(C)** Example segmentation results comparing Cellpose-SAM and the trained General Model on adherent cell images. **(D)** Violin plots of segmentation error rates for Cellpose-SAM versus the Hemocytometer Model (left) and General Model (right), demonstrating improved accuracy with task-specific training. $p < 0.01$, $p < 0.5$. Error Rates were calculated as $(FP+FN)/(TP+FN)$.

Breaking Barriers: A Boosted Osmotic Method for Enhanced Antibody Delivery in Glioblastoma

Shriya Madan[1], Guanda Qiao[1], Shalini Sharma[1], Chengyan Chu[1], David Gulisashvili[1], Lucia Fadon-Padilla[1], Abdallah Salemdawood[1], Joshua Ostovitz[1], Yajie Liang[1], Piotr Walczak[1], Miroslaw Janowski[1]
[1]Department of Diagnostic Radiology, University of Maryland School of Medicine, USA

Introduction- The blood-brain barrier (BBB) presents a major challenge to effective drug delivery for central nervous system (CNS) diseases, particularly glioblastoma (GBM). Osmotic BBB opening (OBBBO) using intra-arterial (IA) infusion of 25% mannitol has been used clinically but offers limited BBB opening territory in small animal models. To address this, we developed a novel boosted OBBBO (BOBBBO) approach combining 25% mannitol with 4% sodium chloride (NaCl) to enhance osmotic strength and expand BBB permeability. This study evaluates the safety, efficacy, and therapeutic potential of BOBBBO in a human xenograft GBM model.

Methods- Tumor progression was monitored via bioluminescence imaging (BLI) and magnetic resonance imaging (MRI). In the fifth week following intracranial tumor implantation, mice underwent BOBBBO using a combination of 25% mannitol and 4% saline, followed by intra-arterial administration of bevacizumab (25 mg/kg). T1-weighted MRI scans were acquired pre- and post-contrast immediately after BOBBBO and again at 3 days to evaluate both safety and efficacy.

Results- BOBBBO reduced the inherent heterogeneity of BBB permeability in GBM, enabling more uniform contrast enhancement in tumor and peritumoral regions. Follow-up MRI at day 3 confirmed the absence of stroke or edema.

Conclusion- BOBBBO using 25% mannitol + 4% NaCl is a safe and effective strategy to enhance BBB opening and therapeutic antibody delivery in mice. It enables broader and more uniform BBB disruption ipsilateral hemispheres of GBM-bearing brains, addressing treatment-limiting heterogeneity. These results support the translational potential of BOBBBO and IA-based delivery approaches, warranting further validation in large-animal models and clinical studies.
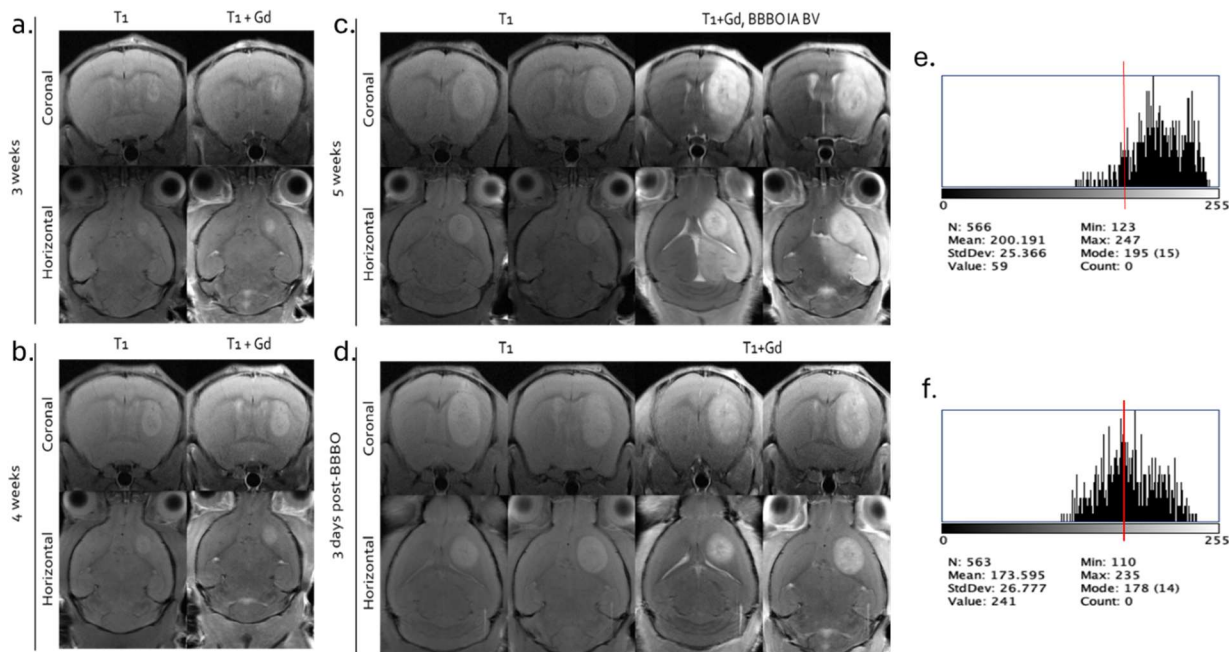

Figure: T1-weighted and contrast-enhanced T1-weighted MRI scans of a GBM1 cell xenograft in the right striatum. (a) and (b) show scans at 3 and 4 weeks post-intracranial transplantation, highlighting initial tumor growth and vascular characteristics. (c) and (d) show scans at week 5, immediately after osmotic blood-brain barrier opening (OBBBO) with intra-arterial bevacizumab (IA BV) administration, and 3 days post-treatment, respectively. (e) and (f) display histograms of pixel intensity values from contrast-enhanced T1-weighted scans in (c) and (d), respectively, illustrating changes in brain contrast uptake reflecting BBB permeability.

High-Temporal-Resolution Monitoring of Cr and PCr Dynamics in Skeletal Muscle by CEST MRI at 3T

Licheng Ju, PhD[1,2], T. Jake Samuel, PhD[2], Michael Schär, PhD[2], Kexin Wang, MS[1,3], Yihan Wu, BS[1,3], Robert G. Weiss, MD[2,4], Jiadi Xu, PhD[1,2]

1. F.M. Kirby Research Center for Functional Brain Imaging, Kennedy Krieger Research Institute, Baltimore, MD, USA
2. Russell H. Morgan Department of Radiology and Radiological Science, Johns Hopkins University School of Medicine, Baltimore, MD, USA
3. Department of Biomedical Engineering, Johns Hopkins University, Baltimore, MD, USA
4. Division of Cardiology, Department of Medicine, Johns Hopkins University School of Medicine, Baltimore, MD, USA

Background

The creatine kinase reaction (CKR) and oxidative phosphorylation (OXPHOS) in muscle have traditionally been assessed through phosphocreatine (PCr) levels using Phosphorus-31 Magnetic Resonance Spectroscopy (^{31}P MRS)[1,2]. Despite its effectiveness, ^{31}P MRS has not been widely adopted in routine clinical practice due to its special hardware requirement. The Chemical Exchange Saturation Transfer (CEST) technique[3,4] has emerged as a promising alternative for detecting low concentrations of Cr and PCr in tissues.

In healthy gastrocnemius muscles, PCr levels demonstrate an exponential recovery post-exercise (with time constant ~30-50 s)[5], which post significant challenges for traditional CEST MRI technique. In our recent paper[6], the temporal resolution of CEST MRI was pushed to 48.6 s using ultrafast Z-spectroscopy (UFZ) method[7]. However, it is still not fast enough and may introduce substantial variability in determining the recovery time constant, especially compared to ^{31}P MRS, which has a temporal resolution of 2 seconds.

Objective

To evaluate the feasibility of high-temporal-resolution (HTR) ultrafast Z-spectroscopy (UFZ) CEST MRI for monitoring dynamic changes in phosphocreatine (PCr) and creatine (Cr) in human skeletal muscle at 3T during and after exercise.

Methods

HTR UFZ-CEST MRI of skeletal muscle was achieved using a 2D turbo spin-echo (TSE) readout with one-dimensional spatial encoding and spectral encoding along the other dimension. Six healthy subjects performed in-magnet plantar flexion exercise, and dynamic changes in amide, phosphocreatine (PCr), and partial PCr-mixed creatine (Cr$^+$) CEST signals during and after exercise were quantified using the PLOF fitting method. This approach enabled monitoring of PCr/Cr dynamics throughout exercise and recovery.

Results

UFZ based CEST MRI achieves a temporal resolution of 7.6 s for high-resolution Z-spectra. Dynamic CEST contrasts revealed PCr depletion and concomitant Cr elevation during exercise, followed by exponential PCr recovery and Cr decay during rest. The post-exercise recovery constants for Cr and PCr CEST were 97.1 ± 31.7 s and 169.8 ± 39.3 s, respectively. Using two-step Bloch-McConnell fitting of PLOF-extracted ΔZ-spectra, we estimated exchange rates of 32.2 ± 22.8 s^{-1} for CrCEST and 175.0 ± 70.5 s^{-1} for PCrCEST.

Conclusions

These results establish UFZ-CEST as a rapid, noninvasive method for mapping Cr/PCr dynamics in human skeletal muscle and provide a foundation for clinical assessment of mitochondrial function.

Figure 1 Dynamic changes in CEST contrasts for a typical subject.

References

1. Isbell DC, etc. J Am Coll Cardiol 2006;47(11):2289-2295.
2. Prompers JJ, etc. NMR Biomed 2006;19(7):927-953.
3. van Zijl PCM, etc. Magn Reson Med 2011;65(4):927-948.
4. van Zijl PCM, etc. Neuroimage 2018;168:222-241.
5. Weiss K, etc. Circ Heart Fail 2017;10(7):e004129.
6. Ju L, etc. Magn Reson Med 2024;30354.
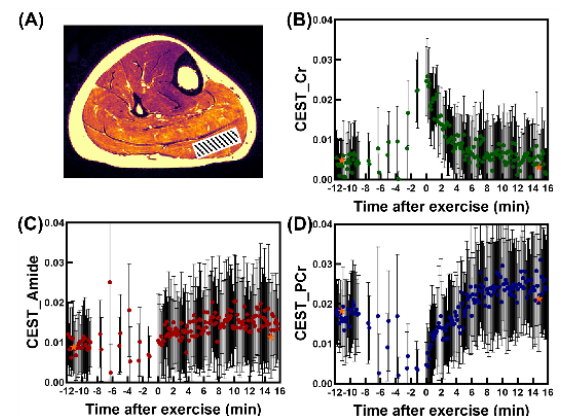7. Xu X, etc. J Magn Reson 2016;265:224-229.

Multimodality Imaging Findings of Takotsubo Syndrome

Jnana Aditya Challa, Youngjae Cha, Recai Aktay

Department of Radiology & Nuclear Medicine, University of Maryland Baltimore

Background

Stress-induced cardiomyopathy, also known as Takotsubo syndrome (TTS), is a transient syndrome characterized by acute ventricular systolic dysfunction often precipitated by emotional or physical stress. TTS is defined by non-obstructive coronary arteries on angiography and imaging findings that typically include apical dyskinetic ballooning of the left ventricle (LV) and basal hyperkinesis. Initially thought to be a self-limiting condition, TTS is now recognized as causing significant short- and long-term morbidity and mortality. TTS patients have higher risk for all-cause and cardiovascular mortality, and major cardiovascular events (about 10%) than the general public, but lower than those with myocardial infarction (MI). Furthermore, recurrence occurs in 1 in 8 patients within five years. It predominantly affects women in their sixth decade of life, but younger patients diagnosed with TTS are more often male, have fewer comorbidities, and frequently present with atypical TTS imaging patterns.

Objective

To discuss the findings and utility of imaging modalities including TTE, CMR, cardiac CT, MPI, MIBG and radionuclide ventriculography in diagnosing TTS and its complications.

Methods

Cases who were suspected to have TTS and underwent TTE, CMRI, CCT, MPI or MUGA scan were reviewed. Representative cases with typical imaging findings of TTS or mimics of TTS were selected.

Results

Some of the cases included are : 1) An adult patient with a history of TTS and ICD placement, subsequently diagnosed with recurrent TTS, 2) A patient who developed TTS shortly after being diagnosed with locally-advanced laryngeal cancer, 3) An adult patient who experienced a fall resulting in multiple facial fractures and a retrobulbar hematoma, initially suspected of having NSTEMI but later diagnosed with TTS following TTE and coronary angiography, 4) An adult patient presenting with acute chest pain and a nonobstructive coronary artery pattern on left heart catheterization, but ultimately found to have a MI pattern on CMRI rather than TTS.
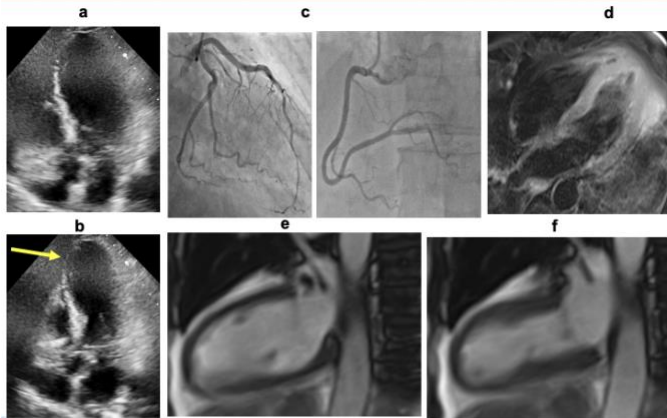
Conclusion

TTS can be challenging to differentiate from acute coronary syndromes due to their similar clinical presentations. However, modern imaging techniques complement the clinical evaluation in diagnosing TTS and guiding management. This educational exhibit presents cases and illustrates the typical imaging features of TTS on multiple imaging modalities.
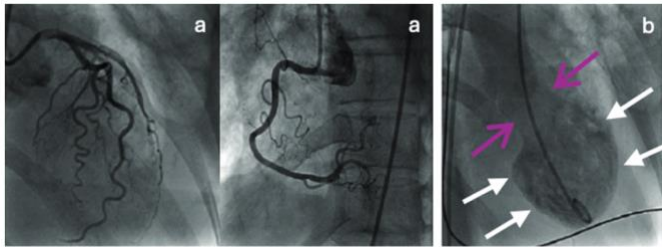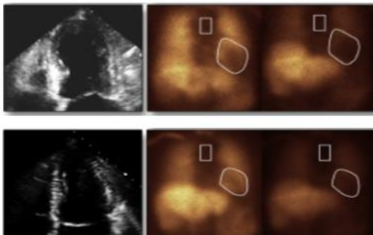
ICA: (a) Normal left and right coronary arteries
Left ventriculogram (b) shows ballooning of LV (white arrows) and preserved contractility at the basal segments.
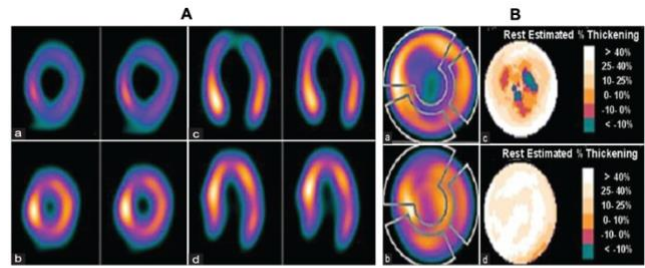
Tc99 MIBI-SPECT images. Early images (Aa, Ac) show decreased myocardial perfusion in distal anterior and lateral wall, and apex. (Ab, Ad) after complete recovery. Bull-eye and thickening images. (Ba-Bc) Acute once. (Bb-Bd) Two months later
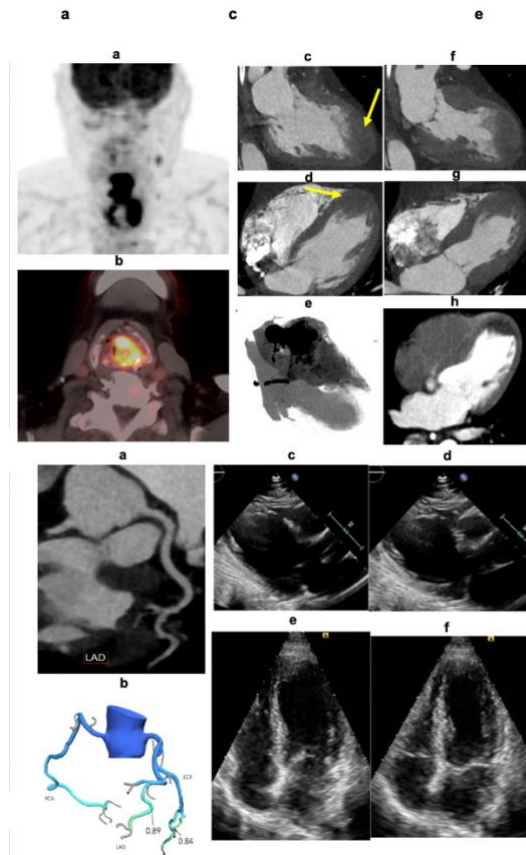

	Subacute	Recovery
LVEF	35%	60%
H/Mlate	1.62	2.42
Wash-out rate	44%	26%
P-epinephrine	71 pg/mL	42 pg/mL
P-norepinephrine	1213 pg/mL	897 pg/mL

Subacute Phase (6-10 days)
End systole   Early-15 min   Late-4 hours
Recovery Phase (4 months)

Takotsubo Group

Developing broadly neutralizing antibody-producing glial progenitors to eradicate Human immunodeficiency virus from the brain.

Lorissa McDougall[1], Abdolrahim Abassi[2], Mohammad Sajadi[2], Alonso Heredia[2], Linda Chang[1], Yajie Liang[1], Chengyan Chu[1], Lukasz Kalkowski[1], Lucia Fadon-Padilla[1], Ben Atkinson[2], Miroslaw Janowski[1], Piotr Walczak[1].

[1]University of Maryland, Baltimore, Department of Radiology and Nuclear Medicine; [2]University of Maryland, Baltimore, Institute of Human Virology.

Background: Antiretroviral therapies (ART) are effective in suppressing viral replication; however, due to low permeability across the blood-brain barrier, clearance of HIV reservoirs from the brain is limited [1]. Thus, to reduce viral spread back into the body, people with HIV require long-term ART, increasing the risk of damage to the liver, kidney and GI tract. Over time, HIV in the brain can also lead to neurological damage due to neuronal loss associated with chronic neuroinflammation [2]. Therefore, there is an urgent need to explore new therapeutic strategies to eliminate HIV from the brain.

Objective: This study utilizes the intrinsic white matter repair properties of glial progenitor cells (GRPs) in repairing HIV-induced neurological damage, while improving their therapeutic capacity via genetic engineering. These modified GRPs produce broadly neutralizing antibodies (bNAb) that bind HIV glycoprotein (gp120) for viral clearance.

Methods: To identify construct transcription and antibody production in the mouse, GRP (mGRP) cells were evaluated with flow cytometry and immunofluorescence of human antibody expressing GFP positive cells. Additionally, we verified bNAb functionality by neutralization and gp120 expressing RAJI binding assays. Lastly, *in vivo* survival of the GRP's was observed via stereotactic intracerebral injection into the brain followed by bioluminescence imaging (BLI) and immunofluorescence of the tissue.

Results: Integration of the lentiviral bNAb constructs (CII and CIII) into the mGRP genome was verified by flow cytometry (GFP reporter) and bNAb staining co-expression in 91.6% of the CII-bNAb-mGRPs and 89.9% of the CIII-bNAb-mGRPs. Immunofluorescence was also identified in 24% of the CII-bNAb-mGRPs and 38% of the CIII-bNAb-mGRPs expressinh the bNAb. A neutralization assay using the purified bNAbs showed >50% viral neutralization by 1.2ug/ml of CII-bNAb and 0.4mg/ml of CIII-bNAb. In addition, a RAJI binding assay found 83% of the RAJI cell population was bound by CII-bNAb while 91% was bound by CIII-bNAb. Finally, *in vivo* intracerebral injection of the GRPs identified cell survival after 72-hours via BLI with 61.7% of cells staining positive for CII-bNAb and 21.6% for CIII-bNAb.
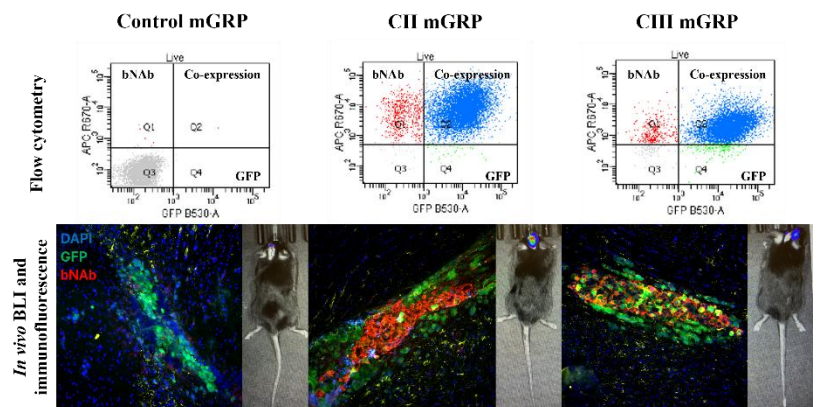
Conclusion: The mGRP cells have been shown to successfully express a stable bNAb which neutralizes viral particles to inhibit infection as well as binding cells expressing the gp120 antigen on the cell surface to aid in clearing infected cells. The mGRPs are also capable of surviving *in vivo* where they release the antibody.

References: [1] Ash, M.K.; Al-Harthi, L.; Schneider, J.R. HIV in the Brain: Identifying Viral Reservoirs and Addressing the Challenges of an HIV Cure. *Vaccines* 2021, *9*, 867. https://doi.org/10.3390/vaccines9080867.

[2] McArthur, Justin C et al. Neurological complications of HIV infection. *The Lancet Neurology* 2005, Volume 4, Issue 9, 543 – 555. https://doi.org/10.1016/S1474-4422(05)70165-4.

Intrahepatic bile leak that mimics gallbladder in HIDA scan: Case report

Jianshu Qi[1], MD, Yousef Fazel[2], MD, Vasken Dilsizian[1], MD, Wengen Chen[1], MD, PhD.

Department of [1]Diagnostic Radiology and Nuclear Medicine, and [2] Gastroenterology, University of Maryland School of Medicine, Baltimore, Maryland

Background: Bile leak into the gallbladder fossa after cholecystectomy is well-known to mimic the gallbladder on imaging; however, intrahepatic bile leak following trauma that mimics the gallbladder on HIDA scintigraphy is uncommon. Timely recognition of such cases can have a significant impact on patient management. Here, we report a case in which an intrahepatic bile leak was initially misidentified as the gallbladder.

Objective: To differentiate between intrahepatic bile leak and gallbladder.

Methods: After intravenous administration of 99mTc-mebrofenin, sequential dynamic abdominal images were obtained over 60 min. Correlate HIDA scan images with other imaging modalities.

Results: A 72-year-old woman sustained a traumatic liver injury. Initial abdominal CT demonstrated liver lacerations involving segments 5 and 8, with a large parenchymal hematoma and active intraparenchymal contrast extravasation from the anterior division of the right portal vein. Follow-up abdominal CT showed interval resorption and decreased size of the parenchymal hematoma, but revealed increasing subcapsular fluid collection and persistent diffuse gallbladder wall edema, raising concern for acute cholecystitis.

HIDA scintigraphy demonstrated a photopenic area in the right hepatic lobe corresponding to the known hepatic laceration on CT. Over time, a round focus of increasing tracer accumulation appeared medial to the photopenic region. This initially mimicked the gallbladder due to its proximity to the usual anatomical location. Correlation with prior coronal CT scans confirmed that this activity represented an intrahepatic bile leak. The gallbladder was not visualized, likely secondary to acalculous cholecystitis. Subsequent ERCP confirmed the intrahepatic bile leak.

CT shows leaking site (red arrow) Leaking site mimicking gallbladder ERCP confirmed bile leak

Conclusions: In this case, the intrahepatic bile leak developed relatively late after the traumatic liver injury, and the leaking site was located very close to the gallbladder, mimicking its appearance. Nevertheless, in the context of traumatic liver injury, a bile leak should always be considered in the differential diagnosis. If an intrahepatic bile leak is suspected during imaging, SPECT can provide additional diagnostic information. Correlation with abdominal CT, particularly coronal views, can serve as an anatomical reference to distinguish a bile leak from the gallbladder, as demonstrated in this case.

CEST MRI based pH and T2 Mapping for Non-invasive Detection of Renal Injury in Methylmalonic Acidemia

Aruna Singh[1,2], Zinia Mohanta[1,2], Irini Manoli,[3] Hilary J. Vernon,[4] Charles P. Venditti,[3] Michael T. McMahon[1,2]

1. *F.M. Kirby Research Center for Functional Brain Imaging, Kennedy Krieger Institute, Baltimore, Maryland, USA*
2. *Russell H. Morgan Department of Radiology and Radiological Science, Johns Hopkins University School of Medicine, Baltimore, Maryland, USA*
3. *Metabolic Medicine Branch, National Human Genome Research Institute, National Institutes of Health (NIH), Bethesda, MD, USA.*
4. *McKusick-Nathans Institute of Genetic Medicine, Department of Pediatrics, The Johns Hopkins University School of Medicine, Baltimore, MD, USA.*

Background:
Renal dysfunction progressing to chronic kidney disease (CKD) is a recognized complication of isolated methylmalonic acidemia (MMA), an inherited organic acidemia caused by methylmalonyl-CoA mutase (MMUT) deficiency.[1] MMA is marked by metabolic instability, multisystem involvement, and high mortality. Early renal involvement is difficult to detect since conventional biomarkers such as serum creatinine and eGFR are unreliable and insensitive to early cellular injury.[2] Multiparametric magnetic resonance imaging (MRI) has emerged as a promising non-invasive approach for assessing renal alterations in CKD.[2-5] Here, we investigated the utility of T2* relaxometry and pH-sensitive CEST MRI in a murine model of MMA under dietary stress.

Methods:
We used a knock-in murine model of MMA (Mmut[p.G715V/pG715V]) harboring a partial-activity MMUT variant. Eight male mice were divided into two groups: regular diet (RD) or high-protein diet (HPD, 45% casein) for six weeks. Body weights were monitored weekly. MRI was performed on an 11.7T scanner with an eight-channel phased-array coil. T2-weighted images were acquired (fat-saturated RARE sequence), and T2* maps were generated using a multi-gradient-echo sequence and Paravision 360. Regions of interest (ROIs) included inner medulla/papilla (IM), inner outer medulla (ILOM), outer outer medulla (OLOM), and cortex (CO). Mean T2* values were calculated and compared using unpaired t-tests, and histogram analysis was performed. For pH mapping, dynamic contrast-enhanced CEST MRI was conducted using a custom diamagnetic agent (imidazole-4,5-dicarboxamide-di-glutamate, I45DC-diGlu), with CEST images acquired at 4.5 and 7.7 ppm and calibrated against in vitro data. Blood and kidney tissues were collected post-imaging for MMA quantification and histology.

Results:
HPD mice showed significant weight loss within two weeks. T2* mapping revealed pronounced hyperintensity, particularly in OLOM, in HPD compared to RD mice. Quantitative analysis showed significantly higher T2* values across all renal regions in HPD (IM: 69.54 ± 13.0 ms; ILOM: 44.49 ± 3.0; OLOM: 46.82 ± 3.4; CO: 33.78 ± 2.1) versus RD (IM: 20.28 ± 6.7; ILOM: 12.96 ± 1.7; OLOM: 13.68 ± 0.9; CO: 9.59 ± 1.2), consistent with diffuse renal involvement. Histogram analysis confirmed broad shifts in T2* distributions. CEST MRI revealed slightly elevated renal pH in HPD mice. The combination of increased T2* and subtle pH elevation likely reflects early renal abnormalities, potentially linked to inflammation, altered perfusion, tissue remodeling, or mitochondrial/tubular dysfunction.

Conclusion:
Our preliminary findings demonstrate that multiparametric MRI, incorporating both relaxation-based and pH-sensitive CEST imaging, can non-invasively detect kidney disease at an early stage, in a murine model of MMA subjected to high-protein dietary stress. Further correlations with biomarkers and renal histopathology are underway.

References:

1. Kruszka PS, Manoli I, Sloan JL, Kopp JB, Venditti CP. Renal growth in isolated methylmalonic acidemia. Genet Med. 2013 Dec;15(12):990-6. doi: 10.1038/gim.2013.42. Epub 2013 May 2. PMID: 23639900; PMCID: PMC4149057.

2. Pavuluri K, Manoli I, Pass A, Li Y, Vernon HJ, Venditti CP, McMahon MT. Noninvasive monitoring of chronic kidney disease using pH and perfusion imaging. Sci Adv. 2019 Aug 14;5(8):eaaw8357. doi: 10.1126/sciadv.aaw8357. PMID: 31453331; PMCID: PMC6693904.

3. Prasad PV, Thacker J, Li LP, Haque M, Li W, Koenigs H, Zhou Y, Sprague SM. Multi-Parametric Evaluation of Chronic Kidney Disease by MRI: A Preliminary Cross-Sectional Study. PLoS One. 2015 Oct 2;10(10):e0139661. doi: 10.1371/journal.pone.0139661. PMID: 26430736; PMCID: PMC4591972.

4. Stabinska J, Singh A, Haney NM, Li Y, Sedaghat F, Kates M, McMahon MT. Noninvasive assessment of renal dynamics and pH in a unilateral ureter obstruction model using DCE MR-CEST urography. Magn Reson Med. 2023 Jan;89(1):343-355. doi: 10.1002/mrm.29436. Epub 2022 Sep 11. PMID: 36089805; PMCID: PMC9753579.

5. Mukherjee S, Bhaduri S, Harwood R, Murray P, Wilm B, Bearon R, Poptani H. Multiparametric MRI based assessment of kidney injury in a mouse model of ischemia reperfusion injury. Sci Rep. 2024 Aug 27;14(1):19922. doi: 10.1038/s41598-024-70401-x. PMID: 39198525; PMCID: PMC11358484.
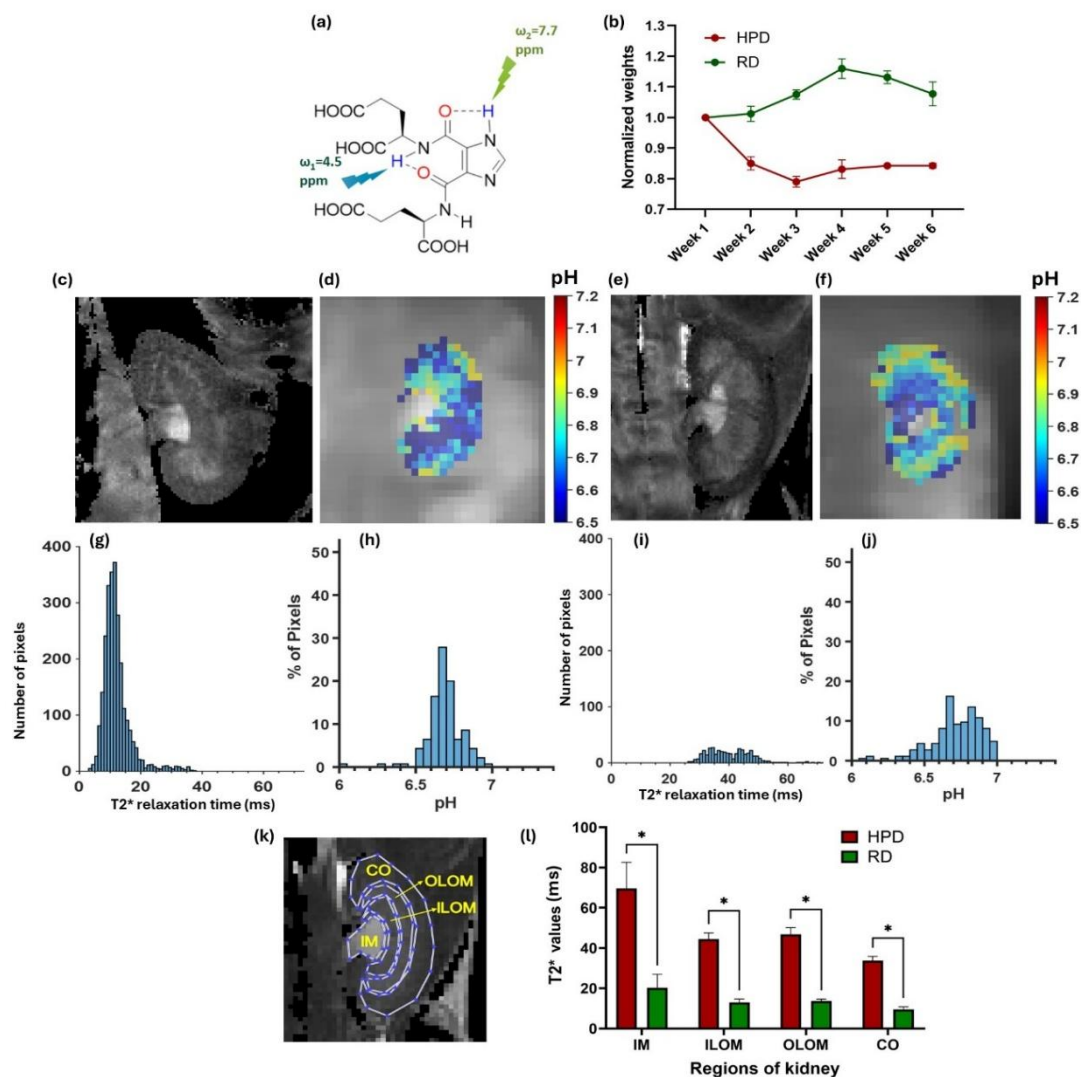
Figure 1: **(a)** Chemical structure of I45DC-diGlu with two pools of exchanging protons resonating at 4.3 and 7.7 ppm; **(b)** Normalized body weights of mice on regular diet (RD) and high-protein diet (HPD) over the study period. Representative $T2^*$ and pH maps from kidney of **(c, d)** a RD mouse; **(e, f)** a HPD mouse. Corresponding histograms of pixel-wise distribution of $T2^*$ values and pH across kidney of **(g, h)** a RD mouse **(i, j)** a HPD mouse; **(k)** Representative T2-weighted anatomical image from a RD mouse kidney showing delineation of four regions of interest (ROIs): inner medulla and papilla (IM), inner layer of outer medulla (ILOM), outer layer of outer medulla (OLOM), and cortex (CO); **(l)** mean $T2^*$ values across renal regions between RD and HPD groups (mean ± SD, $p < 0.05$, n=4).

Design, Synthesis, and Preliminary Evaluation of a New ^{18}F-Labeled Positron Emission Tomography Radiotracer for Indoleamine 2,3-dioxygenase-1 in vivo Neuroimaging

Nilay Narayan, Hua Cheng PhD, Yongle Wang PhD, Changning Wang PhD

Athinoula A. Martinos Center for Biomedical Imaging, Department of Radiology, Massachusetts General Hospital, Harvard Medical School, Charlestown, MA, 02129, USA

BACKGROUND: Indoleamine 2,3-dioxygenase-1 (IDO1) catalyzes the rate limiting step of the kynurenine pathway, which metabolizes tryptophan to quinolinic acid (QUIN). QUIN is implicated in brain damage associated with neurological diseases such as Alzheimer's disease (AD) due to apoptosis in neurons and other harmful processes.[1] Thus, IDO1 is a potential therapeutic target for AD and other neurological disorders. In preclinical studies, IDO1 inhibitors have shown antitumor efficacy. However, the druggability of IDO1 inhibitors for neurological diseases depends on their ability to penetrate the blood-brain barrier (BBB).[2] Therefore, demonstrating that reported IDO1 inhibitors are brain penetrant would extend the potential of these compounds for further biomedical applications such as treating neurological diseases.

OBJECTIVE: To synthesize and radiolabel the IDO1 inhibitor [^{18}F]XW-032 to evaluate its uptake and distribution in various brain regions.

METHODS: A common intermediate (Compound 1) was used to synthesize both a non-radiolabeled XW-032 used as a blocking compound and Compound 2, the precursor to [^{18}F]XW-032. XW-032 was synthesized by coupling Compound 1 with 4-fluoroaniline. To form Compound 2, Compound 1 was coupled with 4-aminophenol. A radiosynthesis was then performed by treating Compound 2 with H^{18}F, replacing the hydroxyl group with ^{18}F. Then, 2 groups of 4 Male BALB/c mice were dosed with 100-200 mCi of [^{18}F]XW-032 (IV) per mice, and a 60-minute PET imaging scan and computed tomography (CT) scan were conducted. To analyze target specificity, a self-blocking study was performed in 2 mice from the first group by injecting non-radiolabeled XW-032 (0.3 mg/kg) 5 minutes before [^{18}F]XW-032 was injected to competitively occupy the binding sites on IDO1. Whole-body regional uptake studies of the mice were also conducted at 5, 15, 30, and 60 minutes, and uptake in discrete brain regions was analyzed.

RESULTS: The results of the PET imaging showed high BBB penetration, with the highest brain uptake value of approximately % ID/CC = 1.9 after injection into mice. The kinetics of [^{18}F]XW-032 in the brain were also favorable, with high uptake observable at 60 min, suggesting strong binding to the IDO1 target protein. When cold XW-032 was co-injected with [^{18}F]XW-032 as a self-blocking compound, a significant reduction in the signal was observed, indicating specific binding to IDO1. The biodistribution of [^{18}F]XW-032 in different brain regions was also analyzed to assess its selectivity. Based on previous IDO1 expression studies, it was expected that [^{18}F]XW-032 should have high uptake in the cortex, and our results confirmed this. The cortex showed the highest uptake of the tracer in addition to the amygdala.

CONCLUSIONS: In this study, we developed [^{18}F]XW-032, a radiolabeled IDO1 inhibitor which showed high brain penetrance, high binding specificity, selectivity in the cortex and the amygdala, and favorable kinetics. These attributes demonstrate that XW-032 is a potent, brain-penetrant IDO1 inhibitor, and establishes [^{18}F]XW-032 as a new PET radiotracer, showing the potential of this class of compounds for probing and treating neurological diseases.

REFERENCES: 1. Kwidzinski, E, Bechmann, I. *J mol med (Berl)*. 2007; *85*(12): 351. **2.** Savonije K, Meek, A, Weaver, DF. *Brain Sci*. 2023; 13(6): 852002E
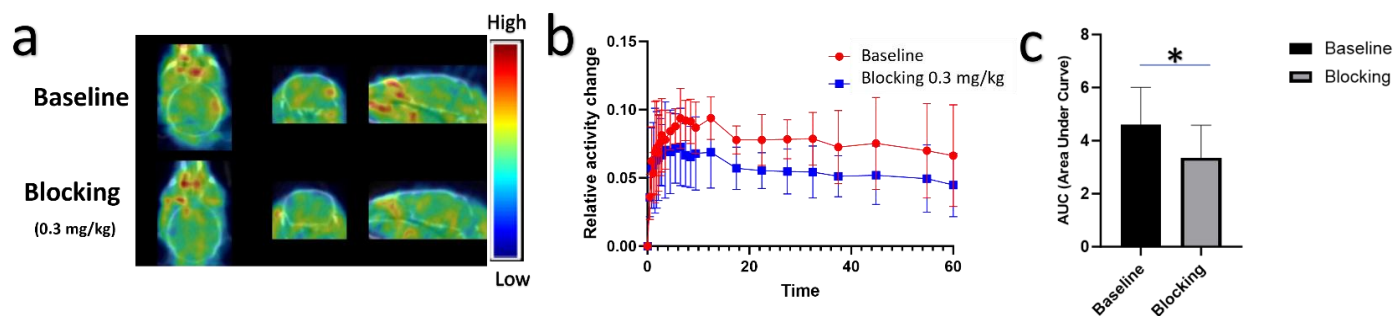
Figure 1. Baseline represents radioactivity in the mice brain when only [^{18}F]XW-032 was injected; blocking represents radioactivity when [^{18}F]XW-032 was injected along with XW-032. (a) PET/CT obtained images of mice brains (20-60 min) of [^{18}F]XW-032. (b) Normalized whole-brain time-activity curves of [^{18}F]XW-032. (c) Area under the curve of standardized uptake value (SUV).

Incidental Simultaneous Detection of Pericardial Effusion and Hyperemic Breast Tissue on Multigated Acquisition (MUGA) Scan

Alireza Amindarolzarbi, MD; Vasken Dilsizian, MD; Wengen Chen, MD, PhD

Department of Diagnostic Radiology and Nuclear Medicine, University of Maryland School of Medicine, Baltimore, MD, USA

Background

Multigated acquisition (MUGA) scans are widely used to assess ventricular function in oncology patients receiving potentially cardiotoxic therapy. Beyond ventricular indices, MUGA can incidentally reveal extra-cardiac findings, some of which may mimic clinically significant pathology. Recognizing these pitfalls and correlating with cross-sectional imaging are essential to avoid misdiagnosis.

Objective

To illustrate the recognition and interpretation of incidental pericardial effusion and anterior chest uptake on baseline MUGA, correlated with cross-sectional imaging.

Methods

A 41-year-old woman with IgA κ multiple myeloma undergoing baseline cardiac function assessment prior to CAR-T therapy had a rest MUGA study performed using 29.7 mCi Tc-99m–labeled red blood cells. Gated acquisitions were obtained in anterior, left anterior oblique (LAO), and lateral views. Findings were compared with chest CT performed within the same 1 month.

Results

MUGA demonstrated normal left ventricular size and systolic function with an ejection fraction of 68%. Two incidental findings were noted:

1. A circumferential photopenic halo around the cardiac blood pool, consistent with pericardial effusion.
2. A diffuse area of increased activity lateral to the left cardiac border in the LAO view, suggestive of tissue with hyperemia.

Chest CT confirmed only a trace pericardial effusion, and large left breast tissue corresponding to the hyperemia area on MUGA; suggestive of inflammatory breast with increased blood flow. The patient remained asymptomatic, and no further interventions were required.

Conclusions

This case underscores the importance of systematic extracardiac evaluation during MUGA interpretation. Pericardial effusion and breast hyperemia can mimic pathology, raising unwarranted concern if unrecognized. Correlation with cross-sectional imaging ensures accurate interpretation, prevents unnecessary workup, and reinforces the critical role of nuclear cardiology in comprehensive oncologic care.
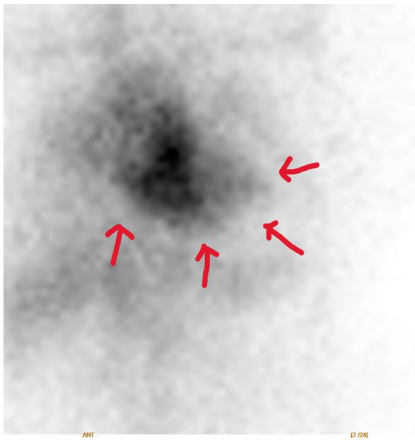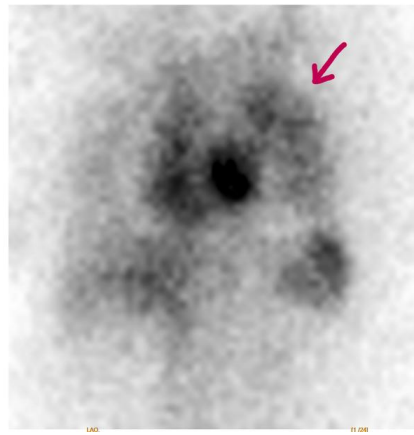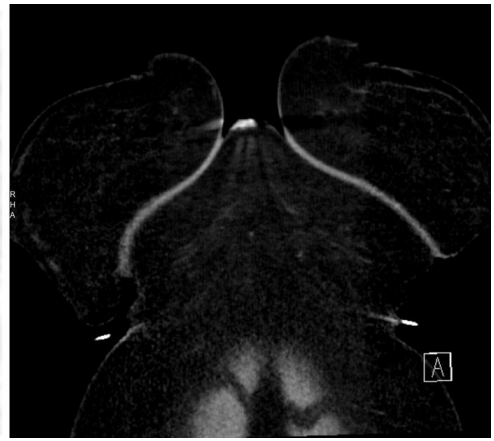
(A)   (B)   (C)

Figure 1. A) Anterior MUGA projection showing photopenia around the cardiac blood pool (arrows) compatible with pericardial effusion. B) LAO projection showing area of diffuse activity lateral to the cardiac border (arrow) correlating to breast tissue on CT. C) Coronal chest CT demonstrating large left breast.

Establishing a platform for high resolution imaging of live tardigrades using a two-photon fluorescence microscope

Hailey Wang, Yajie Liang MD, PhD
Department of Diagnostic Radiology and Nuclear Medicine, University of Maryland School of Medicine

Background: Tardigrades, or *hypsibius exemplaris*, are increasingly used in research as models for neuroscience due to their small but complex features, including a central brain and a peripheral nervous system. Their tractable genome and high stress tolerance create optimal conditions for research.

Objective: To develop a consistent sample preparation and imaging protocol for observation of live tardigrades.

Methods: Tardigrades were both purchased and found in the wild. Moss soaked overnight in bottled water was sieved for large debris and examined under a microscope for movement, and captured tardigrades were relocated via pipette to a cell well. Every week, tardigrades were moved to a new container with fresh spring water and *Chlorococcum* algae. To stain tardigrades with fluorescent Hoechst 33342 dye, tardigrades were incubated for 20-40 minutes at room temperature in 13 µM dye diluted with spring water in the dark. After the staining period, tardigrades were relocated into clean spring water to wash off excess dye before immobilization. For imaging, a circular binder hole sticker was placed on a glass slide, in which a single tardigrade was centered and immobilized by a drop of 2% low melting agarose with a coverslip on top. Microscopes used to image stained and nonstained tardigrades include a Leica wide-field and a two-photon fluorescence microscope. Images were obtained through the microscopes' applications and analyzed using ImageJ.

Results: We managed to immobilize tardigrades using agarose and achieved well-stained samples. We found that longer staining periods created clearer fluorescence in images since the nuclei stain had more time to settle into the tardigrades' cells. However, stained tardigrades in agarose die quickly, so the period between staining and imaging cannot exceed a few hours. As the cells in the tardigrade start to die, the nuclei stain becomes ineffective and can no longer perform effectively. Thus, it is important to stain and image tardigrades in a timely manner for maximum efficiency and productivity in results.

Through the five colored fluorescence channels and 20x zoom feature of the Leica microscope, we were able to image tardigrades with striking detail and precision. However, pressure from the coverslip and slide on the tardigrade caused its abdomen to rupture in both samples, sending fluorescence outside its body. From the non-stained tardigrade, we found that the gut and several parts of the head region were autofluorescent, namely the pharynx, buccal tube, and stylets. The algae in and outside of the tardigrade were most prevalent in the magenta channel. Similarly, the pharynx region of the stained tardigrade was bright but also autofluorescent, shown in the green channel. Bright spots all over the body in the cyan channel show nuclei stained by Hoechst 33342. Images only capture one slice of the whole tardigrade, causing blurred and unclear spots.

The closer zoom and quality of the two-photon fluorescence microscope allowed us to produce high resolution stacks with two channels at different wavelengths. The stained tardigrade may have died during imaging, inferred from its lack of movement; the non-stained tardigrade, however, kept moving when stronger lasers were used, thus causing some unclear images. In both tardigrades, the best quality images were taken at 800 nm. Cell nuclei labeled by Hoechst dye are fluorescent green, while non-labeled parts of the tardigrade are more red, such as the stomach region with the algae inside. As the power increased, the red channel of the stained tardigrade became significantly weaker. On the other hand, the non-stained tardigrade mostly demonstrated autofluorescence around its head region, specifically the pharynx, buccal tube, and stylets.

Conclusions: We were able to establish a platform for high resolution imaging of tardigrades under wide-field and two-photon microscopy, paving a way for using tardigrades as models to study diseases as possible regeneration or injury models.
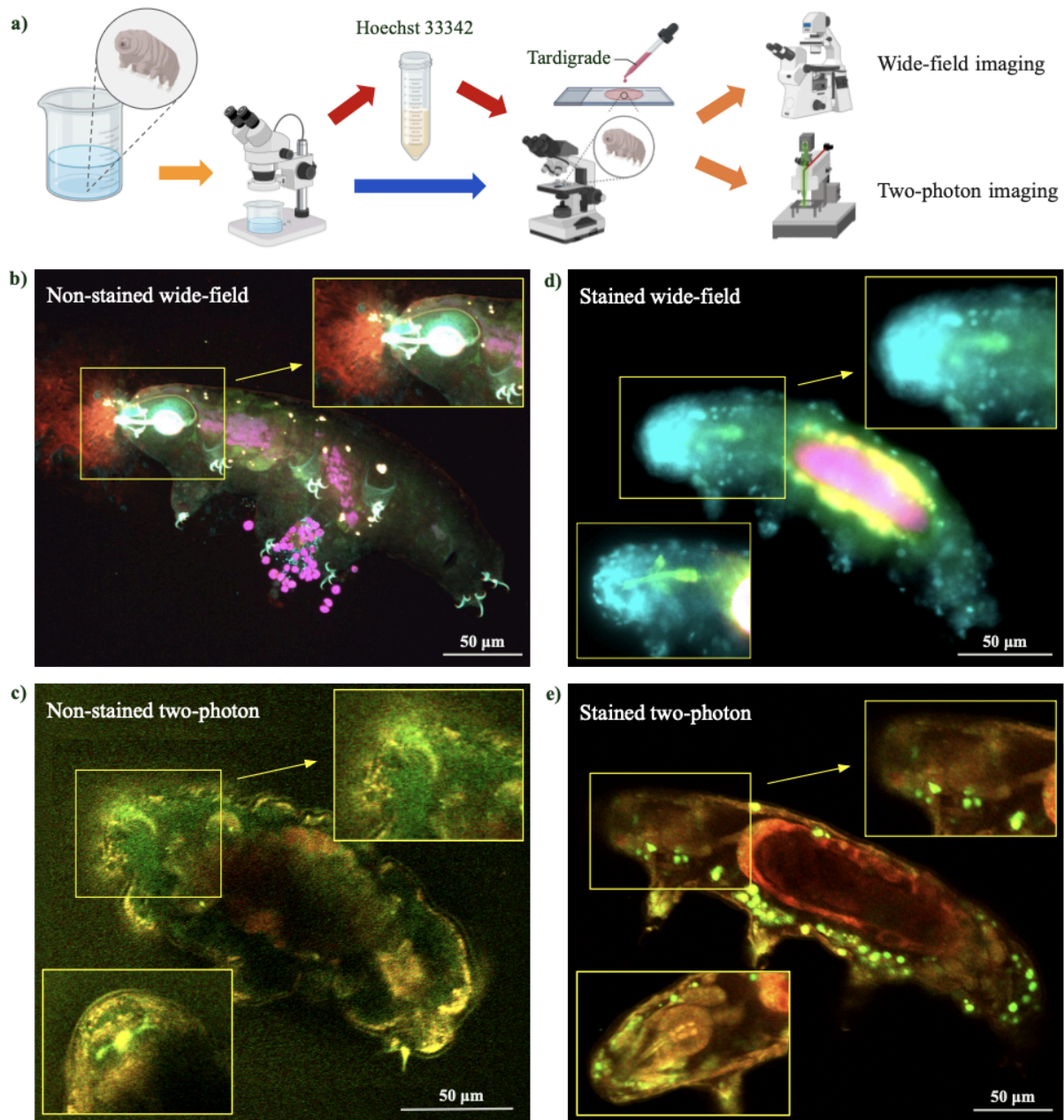
Figure: **a)** Steps involved from obtaining to imaging tardigrades, including harvest, stain, immobilization, and imaging. **b)** Non-stained tardigrade under wide-field microscope showing autofluorescence in pharynx and gut. **c)** Stained tardigrade under wide-field microscope showing clear nucleus dye throughout body. **d)** Non-stained tardigrade under two-photon microscope showing autofluorescence in head region, namely pharynx, though missing part of image due to movement while imaging. **e)** Stained tardigrade under two-photon microscope showing clear dyed green nucleus and autofluorescent gut.

Non-Invasive Monitoring of Brain Metabolic Alterations During Stroke Using Chemical Exchange Saturation Transfer (CEST) MRI: A Multi-Field Study in Two Mouse Models

Kexin Wang, MHS, BS[1,2*], Licheng Ju, PhD[1,3*], Guanda Qiao, MD, PhD[4], Yajie Liang, PhD[4], Yihan Wu, BS[1,2], Chengyan Chu, MD[4], Joshua Rogers, MS[4], Yuguo Li, PhD[1,3], Suyi Cao, MD[5,6], Valina L. Dawson, PhD[5-8], Ted M Dawson, MD, PhD[5,6,7,9], Piotr Walczak, MD, PhD[4], Jiadi Xu, PhD[1,3]

1.F.M. Kirby Research Center for Functional Brain Imaging, Kennedy Krieger Research Institute, Baltimore, MD, USA. 2. Dept. of Biomedical Engineering, Johns Hopkins University (JHU), Baltimore, MD, USA. 3. Russell H. Morgan Department of Radiology and Radiological Science, JHU. 4. Department of Diagnostic Radiology and Nuclear Medicine, University of Maryland School of Medicine, Baltimore, MD, USA. 5. Neuroregeneration and Stem Cell Programs, The Institute of Cell Engineering, JHU. 6. Department of Neurology, JHU. 7. Department of Neuroscience, JHU. 8. Department of Physiology, JHU. 9. Department of Pharmacology and Molecular Sciences, Johns Hopkins University School of Medicine, Baltimore, MD, USA.

Background: During acute ischemic stroke, energy depletion triggers elevated creatine (Cr) levels as a buffer, increased extracellular glutamate from impaired neurotransmitter transport, and a pH drop due to lactic acid buildup. Capturing these metabolic changes is essential for effective intervention, yet current methods fail to simultaneously assess all these alterations. Chemical exchange saturation transfer (CEST) MRI, a promising non-invasive technique, allows high-sensitivity mapping of metabolites, providing both concentration and pH information. Moreover, high-field imaging (9.4T) enhances CEST signal extraction, while low-field imaging (3T) supports clinical translation. Therefore, we conducted 9.4T and 3T scans on mouse stroke models to validate CEST's feasibility in monitoring metabolic alterations and prepare for future clinical applications.

Objective: To validate CEST MRI for detecting metabolic alterations in the brain during stroke across high-field (9.4T) and clinical (3T) scanners. We aimed to determine whether CEST can non-invasively capture changes in key metabolites, neurotransmitters, and pH in two distinct mouse stroke models, providing a foundation for future clinical applications and advancing understanding of stroke-related metabolic dynamics.

Methods: Ten male C57BL/6 mice (3–6 months) underwent permanent (pMCAO) or transient (tMCAO) middle cerebral artery occlusion. Lesions were identified by apparent diffusion coefficient (ADC) maps derived from diffusion-weighted imaging, followed by T_1, T_2, and CEST scans at 9.4T and 3T using matched slice geometry. Saturation was applied across B_1 ranges (0.4~3.0 µT at 9.4T; 0.4~2.0 µT at 3T). Polynomial and Lorentzian Line-shape Fitting (PLOF)[1] extracted GuanCEST, amineCEST (9.4T only), and amideCEST values. In pMCAO, lactate was quantified with ^{1}H MRS to estimate pH changes[2]. Bloch-McConnell simulations modeled expected metabolite and pH effects.

Results: At 9.4T, amineCEST increased significantly in tMCAO (3.86 ± 0.42%) compared to pMCAO (1.09 ± 0.26%), consistent with elevated glutamate. At low B_1, GuanCEST rose in pMCAO (1.01 ± 0.19%) but decreased in tMCAO (-0.32 ± 0.27%), reflecting greater Cr accumulation in pMCAO. AmideCEST changes were minimal in tMCAO but decreased in pMCAO, indicating a larger pH drop. At 3T, GuanCEST increases at low B_1 and amideCEST decreases confirmed stronger acidification in pMCAO. MRS lactate supported these findings, with an estimated pH reduction of ~0.65. Simulations reproduced experimental trends, validating creatine- and amine-related changes.

Figure 1. Representative CEST MRI maps of tMCAO and pMCAO at 9.4T.

Conclusions: CEST MRI distinguishes metabolic responses across stroke models: amine elevation in tMCAO and creatine-associated acidification in pMCAO. These results demonstrate the feasibility of non-invasive, simultaneous mapping of metabolites, neurotransmitters, and pH in stroke, supporting CEST as a promising translational tool for metabolic brain diseases.

Reference: 1. Chen L, et al, *Nature communications* 2020; 11: 1072. 2. Paschen W, et al, *J Neurochem* 1987; 48: 154-159.
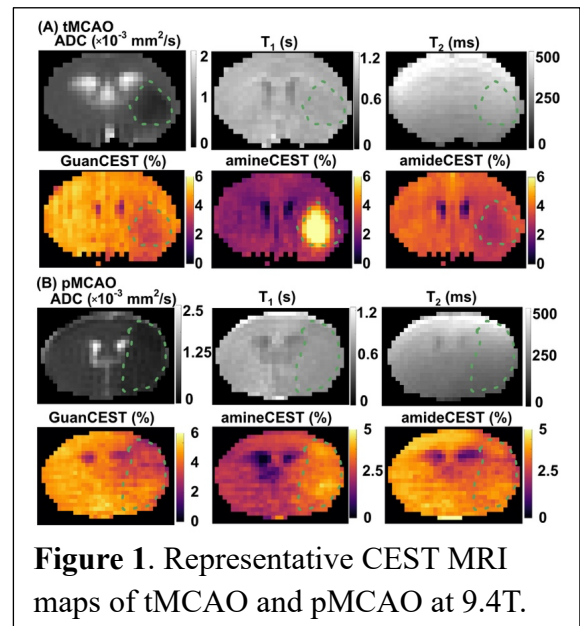
Engineering Extracellular Vesicle-Liposome Hybrids to Support Pancreatic Islet Transplantation in Type 1 Diabetes Treatment

Heng Zhao, PhD, Jeff W. M. Bulte PhD, Dian R. Arifin PhD

Department of Radiology and Radiological Science, Division of MR Research, Johns Hopkins University School of Medicine, Baltimore, MD; Cellular Imaging Section, Institute for Cell Engineering, Johns Hopkins University School of Medicine, Baltimore, MD.

Background: Type 1 diabetes mellitus (T1DM) is a chronic disorder characterized by immune-mediated destruction of pancreatic insulin-producing β-cells. T1DM accounts for 5–10% of diabetic patients in the US. Islet transplantation can provide a long-term glucose control solution for T1DM patients. However, apart from donor islet shortage, islet grafts face loss of viability and function with host immune rejection as one of the leading causes. Human mesenchymal stem cell-derived extracellular vesicles (MSC-EVs) have a great potential to support islet transplantation owing to their anti-inflammatory and immunomodulatory effects. At present, EV therapy is constrained by the limited tunability of EVs and inability to elucidate their fate *in vivo*. Engineering EVs to carry imaging tracers and anti-oxidative agents may improve their function and therapeutic outcome of islet transplantation.

Objective: To develop novel multifunctional liposome-EV hybrids (LPEV) for quantifiable *in vivo* tracking by magnetic particle imaging (MPI), inflammation modulation, and supporting islet transplantation.

Methods: Fusogenic liposomes (FLPs) were prepared through thin-film rehydration to load supersmall anti-oxidative CeO_2 nanozymes and superparamagnetic iron oxide (SPIO) Ferucarbotran nanoparticles (NPs). After incubation and repeated freeze-thaw cycles, EVs were fused with magnetic anti-oxidative liposomes to produce LPEV (**Fig. 1A**).[1]

Results: To confirm EV–liposome fusion, liposomes were dual-labeled with 1,2-dioleoyl-sn-glycero-3-phospho-Lserine-N-(7-nitro-2−1,3-benzoxadiazol-4-yl) (NBD-PS) and 1,2-dioleoylsn-glycero-3-phosphoethanolamine-N-(lissamine rhodamine B sulfonyl) (RhB-PE) and analyzed with a Förster resonant energy transfer
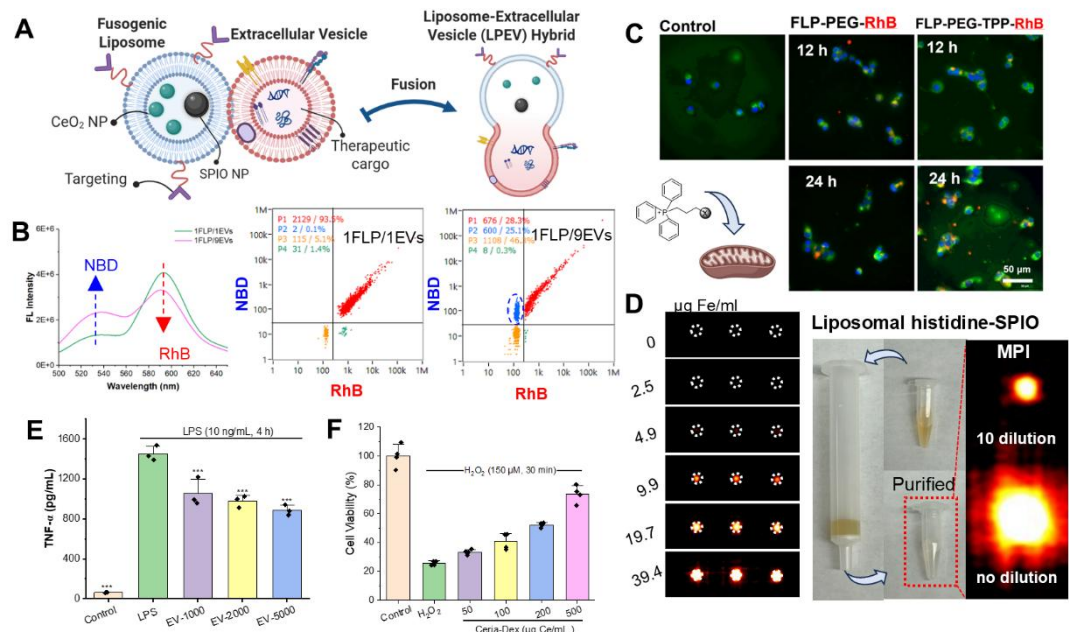

Figure 1 (**A**) Schematic diagram of LPEV preparation. (**B**) Fluorescence (FL) spectra and nanoFCM demonstrating FRET in NBD/RhB-labeled fusogenic liposomes (FLP) mixed with EVs at ratios of 1:1 and 1:9 after 9 freeze-thaw cycles. (**C**) Fluorescent images of FLP with/without TPP (red) internalized by beta (green=mitochondria). Control: cells without FLP. (**D**) MPI phantom image of histidine-Ferucarbotran (SPIO) at various concentrations and liposomal histidine-SPIO. (**E**) Dose-dependent reduction of pro-inflammatory cytokine TNF-α secreted by lipopolysaccharide (LPS, 10 ng/mL)-stimulated Raw 264.7 macrophages after MSC-EV treatment (0, 1k, 2k and 5k EVs/macrophage). Control: macrophages without LPS and EV treatment. (**F**) Cell viability of beta-TC6 cells after hydrogen peroxide exposure (150 μM for 30 min) with Ceria-Dextran (or without as control).

(FRET) dequenching assay (**Fig. 1B**). Donor fluorophore NBD and acceptor RhB intensity changed with liposome/EV ratio, consistent with the fused membranes diluting the FRET dyes to respectively enhance and attenuate the donor and acceptor signal. Our next step was to optimize the different parts of LPEV prior to LPEV synthesis. **Fig. 1C** demonstrates that while FLP without (FLP-PEG-RhB) or with mitochondria-targeting TPP (Triphenylphosphonium) FLP-PEG-TPP-RhB were internalized by murine insulinoma Beta-TC6 cells. FLP-PEG-TPP-RhB exhibited a stronger red signal that merged with the green signal from MitoTracker Green (stained mitochondria). We have successfully tagged histidine to Ferucarbotran, loaded these into FLP and removed unencapsuled ferucabotran by Ni-NTA columns (to eliminate false signals from free tracers). Liposomal histidine-SPIO (**Fig. 1D**) appeared as "hot spots" on MPI. EVs (**Fig. 1E**) and CeO_2NPs (**Fig. 1F**) showed dose-dependent anti-inflammatory and anti-oxidative effects.

Conclusion: We demonstrated successful fusion of EVs and liposomes. Magnetic liposomes can be detected by MPI, and EVs and CeO_2 NPs can modulate inflammation and oxidative damage associated with the failure of islet transplantation.

References: 1. Hettich, B. F et al. Adv. Healthcare Mater. **2022**, 11, 2100047

Metabolic Glycoengineering Confers CEST MRI Visibility to Extracellular Vesicles.

Safiya Aafreen[1], MSE, Kris Dammen-Brower[1], MSE, Wenshu Qian[2,3], PhD, Wenshen Wang[2,3], PhD, Wenying Jiang[2,3], MD, Sixuan Li[4], PhD, Xiaoning Han[5], PhD, Tza-Huei Wang[4], PhD, Kevin J. Yarema[1], PhD, Guanshu Liu[2,3], PhD.

1. Department of Biomedical Engineering, Johns Hopkins University, Baltimore, MD. 2. F.M. Kirby Research Center for Functional Brain Imaging, Kennedy Krieger Institute, Baltimore, MD. 3. Russell H. Morgan Department of Radiology and Radiological Science, Johns Hopkins University School of Medicine, Baltimore, MD. 4. Department of Mechanical Engineering, Johns Hopkins University, Baltimore, MD.5. Department of Anesthesiology and Critical Care Medicine, Johns Hopkins University, Baltimore, MD, USA.

Background: Extracellular vesicles (EVs) hold promise as neurotherapeutic carriers, but translation is limited by the lack of non-invasive tracking methods. We applied metabolic glycoengineering (MGE) with the azido-sugar 1,3,4-O-Tri-butyrate-N-azidoacetylmannosamine (ManNAz) to generate EVs enriched with azido-sialic acids (Az-Sia)[1]. These engineered EVs are proposed to be both chemically clickable and detectable by Chemical Exchange Saturation Transfer (CEST) MRI. This platform potentially enables versatile imaging and therapeutic applications.

Objective: To develop metabolically glycoengineered, chemically clickable EVs with distinct CEST MRI signatures for non-invasive in vivo tracking.

Methods: Human ReNcell VM neural progenitor cells (NPCs) (5×10^6, Sigma-Aldrich) were cultured for 48h in medium containing 250 µM ManNAz (MW 472.5 Da, Fig. 1A) to promote Az-Sia incorporation. EVs were harvested via qEV size-exclusion columns (IZON Gen 2) and characterized in accordance with MISEV2023 guidelines[2]. Surface sialylation was quantified by periodate–resorcinol assays, and azide incorporation validated by CICS/SN-FSHS[3]. CEST properties of ManNAz (100 mM, 33% ethanol) and MGE-EVs ($\sim 10^8$/mL, pH 6–8) were benchmarked against glucose on a Bruker 11.7T vertical scanner (RARE sequence, B_1=1.2–5.9 µT, Tsat=4s, TR/TE=6s/5 ms).

For in vivo studies, C57Bl/6J mice (n=5) received bilateral intracranial injections of either EVs or cells. For EVs, native EVs ($\sim 10^8$ particles, left hemisphere) and MGE-EVs ($\sim 10^8$ particles, right hemisphere) were delivered in 3 µL HAMC hydrogel (1% HA, 2% MC) at 0.3 µL/min. For cells, native NPCs (1×10^4, left) and MGE-NSCs (1×10^4, right) were similarly injected. CEST MRI was performed 3 h post-injection on a Bruker 11.7T horizontal scanner (B_1=1.8 µT, Tsat=3s, $\Delta\omega$=–4 to +4 ppm, 0.1 ppm steps), and Z-spectra/MTRasym maps were generated after B_0 correction (WASSR). Histological sections were stained with DBCO–Alexa Fluor 647 (azides) and anti-human CD63 to localize EVs and NSCs, respectively.

Results: Metabolic glycoengineering (MGE) effectively incorporated azido-sialic acids into both cells and EVs. Biochemical assays and single-particle analysis demonstrated nearly two-fold greater Az-Sia enrichment compared to commercial ManNAz (Figs. 1B–C), without altering morphology (TEM, Fig. 1D). The azido-sugar precursor, ManNAz, exhibited a distinct and concentration-dependent CEST effect in vitro (Figs. 1E-G), confirming its suitability as an MRI-detectable chemical handle. For EVs, MGE-EVs produced strong CEST contrast detectable at concentrations as low as 10^8 EV/mL (0.166 pM), far below therapeutic dosing levels, whereas native EVs showed negligible signals (Fig. 1H).In supportive studies, MGE-NSCs generated robust CEST MRI signals following intracranial injection, while native NSCs produced negligible contrast. Histological staining with DBCO–Alexa Fluor 647 further confirmed azide-specific labelling in brain tissue (Fig. 1I), validating the feasibility of tracking glycoengineered cells in vivo. Intracranial injection of MGE-EVs resulted in significantly higher MRI contrast than native EVs (MTR_{asymm} = 1.53 ± 0.31% vs. 0.93 ± 0.42%, P = 0.0117; Fig. 1H). Histological staining corroborated MRI findings, demonstrating spatial localization of MGE-EVs in mouse brains (Fig. 1I).

Conclusion: Metabolic glycoengineering enables ultrasensitive CEST MRI detection of both transplanted cells and their secreted EVs. While supportive cell experiments establish feasibility, the primary innovation provides the first demonstration of MGE-EVs having a strong, non-invasive CEST MRI contrast at clinically relevant doses. This platform offers a promising path toward real-time tracking of EV-based therapeutics *in vivo*.

References: 1. Dammen-Brower, K. et al. Front Chem 10, 863118 (2022). 2. A Welsh, J. et al. J Extracell Vesicles 13(2), e12404 (2024). 3. Li, S. et al. ACS Nano 18, 15729-15743 (2024).
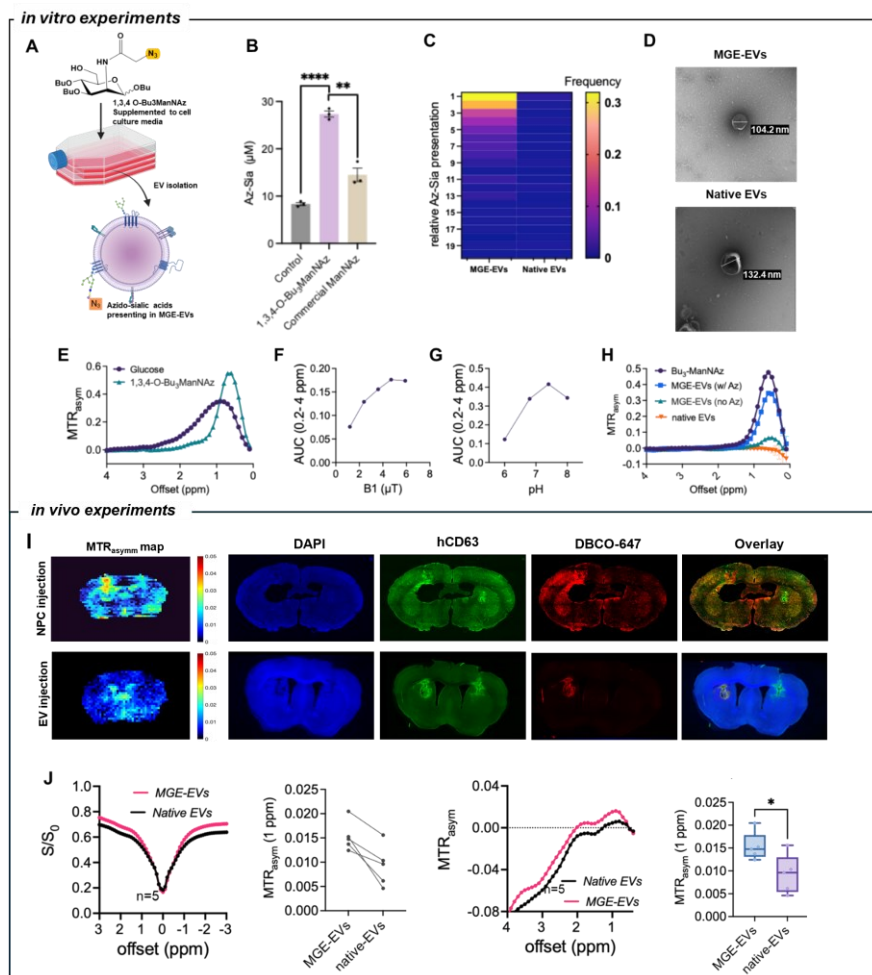
Figure 1 *in vitro* and *in vivo* detection of MGE-EVs using CEST MRI. (**A**) Schematic of MGE-EV preparation. (**B**) Resorcinol assay of sialic acid incorporation. (**C**) Single-particle analysis of azide enrichment. (**D**) TEM images showing preserved morphology. (**E**) MTR_{asymm} CEST profile of ManNAz compared to glucose. (**F**) B_1 dependence and (**G**) pH dependence of the ManNAz CEST signal. (**H**) MTR_{asymm} plots of MGE-EVs and native EVs. (**I**) In vivo CEST MRI at 1.0 ppm with corresponding histological images of bilateral intracranial (MGE left , native right) of NPC cells and EVs (DAPI, CD63, DBCO-AF647, overlays). (**J**) Quantification of ROI mean MTR_{asymm} signals (n=5).

A Non-Genetic EV Labeling Method for Bioluminescence Imaging

Wenshen Wang[1,2], Safiya Aafreen[1,2,3], Olesia Gololobova[4], Kenneth W. Witwer[4], Guanshu Liu[1,2]

1. F.M. Kirby Research Center, Kennedy Krieger Institute; 2. Department of Radiology, Johns Hopkins University; 3. Department of Biomedical Engineering, Johns Hopkins University; 4, Department of Molecular and Comparative Pathobiology, Johns Hopkins University.

Background

Extracellular vesicles (EVs) are crucial natural nanoparticles facilitating cell-to-cell communication by transferring bioactive cargo[1]. Efficient in vivo imaging tools for EV tracking are essential to advance our understanding of EV functions and to facilitate their therapeutic use. Bioluminescence imaging (BLI) offers high sensitivity for preclinical tracking. Traditionally, BLI labeling of EVs involves genetic engineering of cells to produce fusion proteins of luciferase like NanoLuc attached to EV markers (e.g., CD63, CD9, or CD81). Advanced reporters like PalmGRET[2], which combines a palmitoylation signal peptide sequence with an EGFP-NanoLuc BRET pair, enable efficient and pan labeling of EVs of different sizes. However, all of the previously reported methods require genetic modification of EV-producing cells, a process that is time-consuming and requires expertise, limiting their broad applicability.

Objective

Here, we present a novel, non-genetic method for bioluminescent EV labeling by fusing target EVs with PalmGRET-expressing EVs, offering a simple and universal way to create EVs with "bioluminescent labeling by fusion" (BLF-EVs). Demonstrated on tumor-EVs, the preliminary data revealed that BLF-EVs possess sensitive, quantitative BLI signals, suggesting their potential as a versatile EV tracking platform.

Materials and Methods: EVs derived from cell culture were isolated from conditioned media using size exclusion chromatography with qEV columns (70 nm, IZON) and characterized according to MISEV2023 guidelines[3]. Nanoluc-EVs were derived from palmGRET-expressing Expi293F cells[4], while tumor-EVs were collected from cultured 4T1 murine breast tumor cells. BLF-EVs were prepared by extruding the mixture of Nanoluc-EVs and 4T1-EVs at a ratio of 1:10 using an AVESTIN LipoFast system, first through a 100 nm film, then a 50 nm film (**Fig. 1A**)[5]. The success of the fusion of using Memglow488-labeled Nanoluc-EVs and Memglow640-labeled 4T1-EVs was confirmed by nano-flow cytometry (NanoFCM). *In vitro* and *in vivo* BLI studies were performed using a Caliper IVIS SpectrumCT In Vivo Imaging System. In vivo demonstration was conducted in mice subcutaneously injected with different numbers of BLF-EVs.

Results and Discussion: TEM results (**Fig. 1B**) reveal the preserved morphology and integrity of BLF-4T1-EVs compared to parental 4T1-EVs, with size reduced to approximately 70 nm due to the extrusion process. Fusion efficiency was confirmed by the presence of dual-positive particles in NanoFCM (**Fig. 1C**). The resulting BLF-4T1-EVs exhibited a strong BLI signal upon incubation with substrate 10 µM Fluorofurimazine (FFz). Based on the vitro BLI measurement, we estimated the limit of detection (LOD) was $\sim 1 \times 10^9$ EV/mL (**Fig. 1D, E**). Following intravenous injection of FFz, distinct and quantifiable bioluminescent signals were detected for those sites locally injected with 5×10^9 and 1×10^{10} particles in mice (**Fig. 1F**). Dynamic study showed that the signal intensity increased rapidly within the first 8 min and reached the peak intensity approximately 12 min after substrate administration. (**Fig. 1G**). The BLI signal is found to be linearly related to EV concentrations at the high concentration regime (**Fig. 1H**).

Conclusions: A novel EV labeling approach, called Bioluminescent labeling by fusion (BLF), was invented and showcased using 4T1-EVs. Both in vitro and in vivo imaging studies revealed strong, quantitative BLI signals from BLF-EVs, providing a viable alternative to conventional genetic engineering methods for generating BLI-trackable EVs.
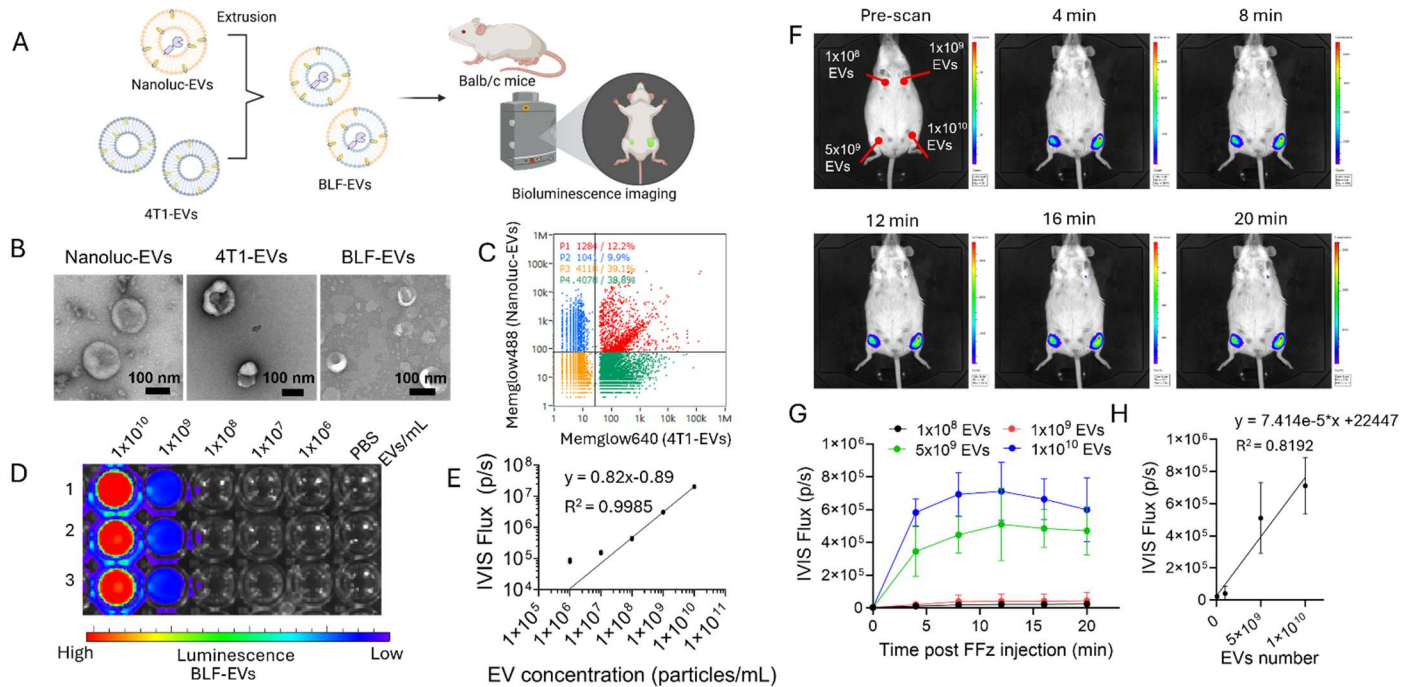
Figure 1

Figure 1. (**A**) Schematic of bioluminescent labeling of 4T1-EVs through extrusion-induced fusion. (**B**) TEM pictures of Nanoluc-EVs, 4T1-EVs and BLF-EVs. (**C**) NanoFCM result showing fusion of Memglow488-labeled Nanoluc-EVs and Memglow640-labeled 4T1-EVs. (**D**) BLI image of serially diluted BLF-EVs from 96-well plate acquired with IVIS Spectrum Imaging System. (**E**) Correlation between luciferase activity and EV concentration acquired by IVIS Spectrum Imaging System. (**F**) Dynamic BLI locally injected BLF-4T1-EVs at different concentrations at different time points of substrate FFz injection. (**G**) Dynamic curves of BLI signal at the sites injected with different EV concentrations (n=3). (**H**) Correlation between bioluminescent signal and EV number intensity at 12 minutes post-administration of FFz. For correlation, show all data points, make it a scatter plot, then show the linear correlation coefficient.

References

[1] D. Gupta, X. Liang, S. Pavlova, O.P.B. Wiklander, G. Corso, Y. Zhao, O. Saher, J. Bost, A.M. Zickler, A. Piffko, C.L. Maire, F.L. Ricklefs, O. Gustafsson, V.C. Llorente, M.O. Gustafsson, R.B. Bostancioglu, D.R. Mamand, D.W. Hagey, A. Gorgens, J.Z. Nordin, S. El Andaloussi, Quantification of extracellular vesicles in vitro and in vivo using sensitive bioluminescence imaging, J Extracell Vesicles 9(1) (2020) 1800222.

[2] A.Y. Wu, Y.C. Sung, Y.J. Chen, S.T. Chou, V. Guo, J.C. Chien, J.J. Ko, A.L. Yang, H.C. Huang, J.C. Chuang, S. Wu, M.R. Ho, M. Ericsson, W.W. Lin, C.H.Y. Cheung, H.F. Juan, K. Ueda, Y. Chen, C.P. Lai, Multiresolution Imaging Using Bioluminescence Resonance Energy Transfer Identifies Distinct Biodistribution Profiles of Extracellular Vesicles and Exomeres with Redirected Tropism, Adv Sci (Weinh) 7(19) (2020) 2001467.

[3] J.A. Welsh, D.C.I. Goberdhan, L. O'Driscoll, E.I. Buzas, C. Blenkiron, B. Bussolati, H. Cai, D. Di Vizio, T.A.P. Driedonks, U. Erdbrugger, J.M. Falcon-Perez, Q.L. Fu, A.F. Hill, M. Lenassi, S.K. Lim, M.G. Mahoney, S. Mohanty, A. Moller, R. Nieuwland, T. Ochiya, S. Sahoo, A.C. Torrecilhas, L. Zheng, A. Zijlstra, S. Abuelreich, R. Bagabas, P. Bergese, E.M. Bridges, M. Brucale, D. Burger, R.P. Carney, E. Cocucci, R. Crescitelli, E. Hanser, A.L. Harris, N.J. Haughey, A. Hendrix, A.R. Ivanov, T. Jovanovic-Talisman, N.A. Kruh-Garcia, V. Ku'ulei-Lyn Faustino, D. Kyburz, C. Lasser, K.M. Lennon, J. Lotvall, A.L. Maddox, E.S. Martens-Uzunova, R.R. Mizenko, L.A. Newman, A. Ridolfi, E. Rohde, T. Rojalin, A. Rowland, A. Saftics, U.S. Sandau, J.A. Saugstad, F. Shekari, S. Swift, D. Ter-Ovanesyan, J.P. Tosar, Z. Useckaite, F. Valle, Z. Varga, E. van der Pol, M.J.C. van Herwijnen, M.H.M. Wauben, A.M. Wehman, S. Williams, A. Zendrini, A.J. Zimmerman, M. Consortium, C. Thery, K.W. Witwer, Minimal information for studies of extracellular vesicles (MISEV2023): From basic to advanced approaches, J Extracell Vesicles 13(2) (2024) e12404.

[4] T. Driedonks, L. Jiang, B. Carlson, Z. Han, G. Liu, S.E. Queen, E.N. Shirk, O. Gololobova, Z. Liao, L.H. Nyberg, G. Lima, L. Paniushkina, M. Garcia-Contreras, K. Schonvisky, N. Castell, M. Stover, S. Guerrero-Martin, R. Richardson, B. Smith, V. Machairaki, C.P. Lai, J.M. Izzi, E.K. Hutchinson, K.A.M. Pate, K.W. Witwer, Pharmacokinetics and biodistribution of extracellular vesicles administered intravenously and intranasally to Macaca nemestrina, J Extracell Biol 1(10) (2022).
[5] Y.Y. Jhan, D. Prasca-Chamorro, G. Palou Zuniga, D.M. Moore, S. Arun Kumar, A.K. Gaharwar, C.J. Bishop, Engineered extracellular vesicles with synthetic lipids via membrane fusion to establish efficient gene delivery, Int J Pharm 573 (2020) 118802.

Microneedle array enables broader cortical dispersion compared with Hamilton syringe

Honglin Tan[1], Michela Sanguedolce[2], Jinghui Wang[1], Kinneret Rand-Yadin[2], Miroslaw Janowski[1], Piotr Walczak[1], Ryan D Sochol[2], Yajie Liang[1]

[1]Diagnostic Radiology and Nuclear Medicine, University of Maryland School of Medicine, Baltimore, MD
[2]Department of Mechanical Engineering, University of Maryland, College Park, MD

Background: Microneedle array (MNA) has emerged as a minimally invasive tool for spatially multiplexed and localized delivery into brain tissue, and recent advances in hybrid micro-/nanoprinting now enable fabrication of precise hollow designs suitable for intracerebral applications [1,2]. Nevertheless, their intracerebral dispersion characteristics have not been systematically validated, and their utility for viral vector delivery remains largely uncharacterized.

Objective: To assess MNA-mediated dispersion using gel and ex vivo cortex models, and to compare in vivo cortical distribution and lentiviral transduction efficiency with Hamilton syringe injection.

Methods: A custom-fabricated hollow microneedle array was characterized (Fig. 1A). To visualize dispersion, Evans blue was aspirated and injected into 1% agarose gel (Fig. 1B–D) and into ex vivo mouse cortex (Fig. 1E–H). For vivo experiments, adult mice received bilateral injections of a GFP-expressing LeGO-G2 lentivirus driven by the SFFV promoter. The left hemisphere was injected via the MNA (Fig. 1I–K), while the right hemisphere was injected with a 33-gauge Hamilton syringe at depths of 0.6 or 0.8 mm (Fig. 1I). One-week post-injection, brain sections were examined by fluorescence microscopy (Fig. 1L–O), and GFP signals were cross-checked against the red channel to distinguish true GFP expression from tissue autofluorescence.

Results: Evans blue injection demonstrated that MNA delivery produced broader and more distributed deposition patterns in both 1% agarose gel and ex vivo mouse cortex (Fig. 1B–H). These findings confirmed that MNAs enable broader and more distributed delivery in gel and ex vivo cortex. In vivo, GFP-positive cells were detected only in Hamilton-injected hemispheres at an injection depth of 0.8 mm, with viral spread observed in the corpus callosum (Fig. 1L–M, white arrows). In contrast, MNA-injected hemispheres showed signals restricted to needle tracks (Fig. 1N) that overlapped with the red channel upon magnification (Fig. 1O, yellow arrowheads), consistent with tissue autofluorescence rather than true transgene expression. The lack of widespread expression of GFP may be due to the SFFV promoter being inactive in neurons, but it's active in proliferating cells such as neural stem cells and oligodendrocyte precursor cells. These findings underscore the distribution potential of MNA and point to the need for neuron-permissive promoters and optimized penetration depth to achieve effective cortical targeting.

Conclusion: These results confirm that microneedle arrays can deliver fluids and viral vectors into a wide range of brain regions, supporting their potential as minimally invasive tools for intracerebral applications. Further characterization and optimization are required to fully establish their efficacy for cortical gene delivery.

References:
1. S. Sarker et al., Adv Mater Technol 8, (2023).
2. S. Sarker et al., Proc IEEE Int Conf Micro Electro Mech Syst 2024, 429-432 (2024).
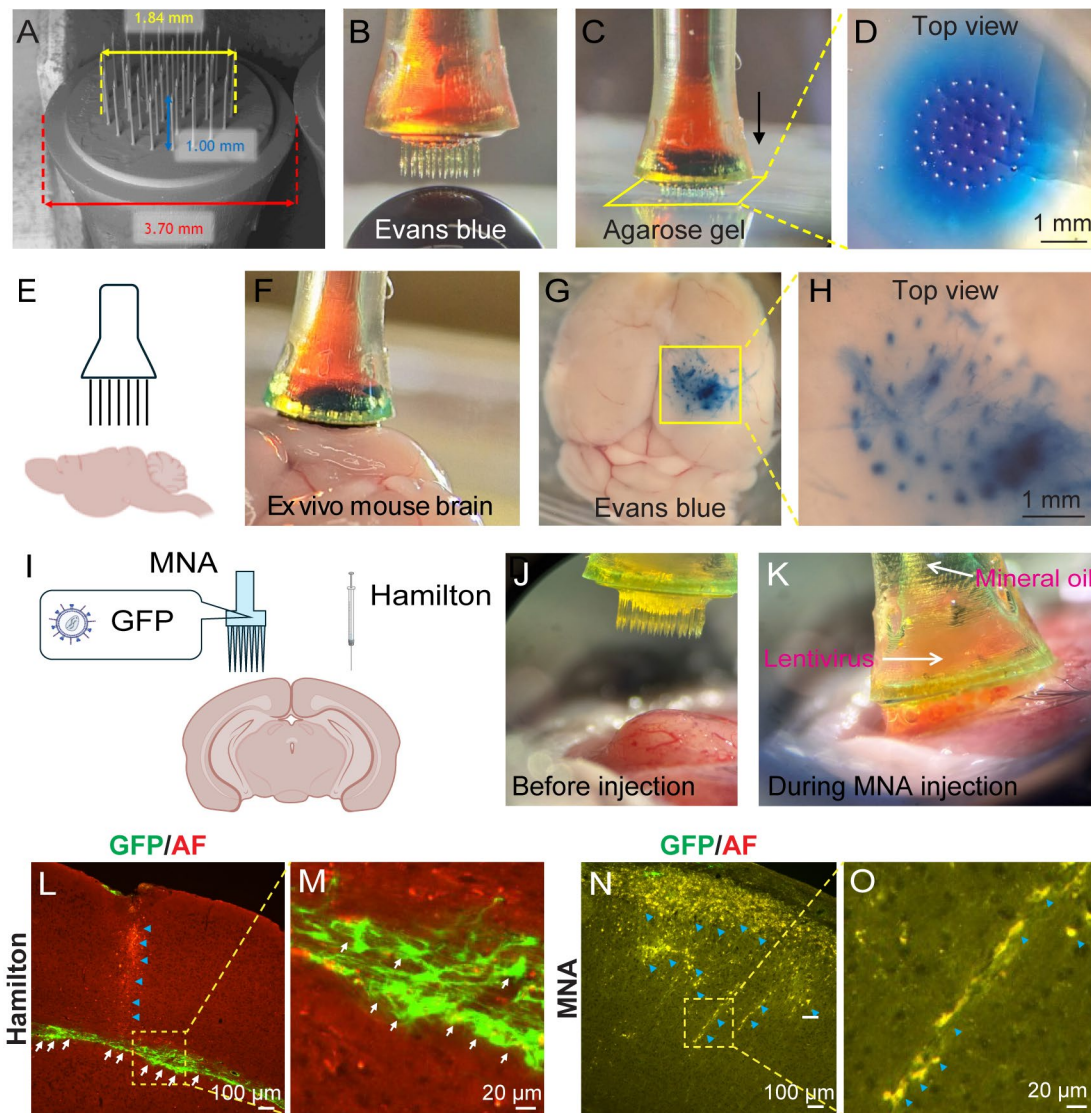
Figure 1. Evaluation of microneedle array (MNA) delivery and comparison with Hamilton syringe injection.

(A) Custom-fabricated hollow MNA with 41 microneedles (1 mm length, 50 μm internal diameter). (B–D) Evans blue injection into 1% agarose gel showing distributed deposition. (E–H) Evans blue injection into ex vivo mouse cortex demonstrating broader dispersion. (I–K) Bilateral in vivo design: the left hemisphere was injected with MNA (1.4 μL over 1.5 min, 0.6 mm depth), and the right with a 33-gauge Hamilton syringe (1.4 μL at 1.0 μL/min, depths of 0.6 or 0.8 mm). (L–M) Representative images from the 0.8 mm Hamilton injection, showing GFP-positive cells in the corpus callosum (white arrows); no CC labeling was observed at 0.6 mm depth. (N–O) MNA injection at 0.6 mm produced green signals restricted to needle tracks that overlapped with red autofluorescence (AF, blue arrowheads).

In vivo imaging the onset of hypoperfusion in mouse brain enabled by remotely controlled micro-balloons

Jinghui Wang[1], Jong Bin Kim[2], Guanda Qiao[1], Honglin Tan[1], Miroslaw Janowski[1], Shu Yang[2], Piotr Walczak[1], and Yajie Liang[1]

[1] Department of Diagnostic Radiology and Nuclear Medicine, University of Maryland School of Medicine, Baltimore, MD.
[2] Department of Material Science and Engineering, University of Pennsylvania, 3231 Walnut Street, Philadelphia, PA 19104, USA. Corresponding author: Yajie.liang@som.umaryland.edu

Background

Ischemic stroke is a major cause of death and disability worldwide. However, current small animal models do not permit continuous imaging during the peri-stroke period, limiting the ability to capture dynamic pathophysiological events essential for understanding stroke onset and recovery.

Objective

To establish MRI-compatible, remote micro-balloon control of cerebral blood flow in mice, enabling continuous imaging during cerebral ischemia and reperfusion.

Methods

Adult mice were anesthetized with isoflurane. A midline neck incision was made to expose both common carotid arteries (CCAs). The left CCA was permanently occluded, and a custom micro-balloon connected to a syringe was positioned around the right CCA (**Fig 1a**). Stepwise balloon inflation allowed reversible occlusion. Cerebral blood flow was monitored by laser Doppler, with additional two-photon imaging through a cranial window and MRI performed to assess perfusion and oxygenation dynamics (BOLD effect).

Results

The micro-balloon system enabled controlled and reversible occlusion of the mouse common carotid artery, providing a highly flexible ischemia–reperfusion model. Stepwise inflation led to progressive narrowing of the vascular lumen, ranging from partial to complete blockage, while sustained inflation produced stable ischemia (**Fig. 1a**). Two-photon line-scan imaging of cortical microvasculature further revealed a sharp decline in capillary flow velocity during inflation, which rapidly recovered after balloon release (**Fig. 1b-c**). MRI experimental design enabled systematic assessment of perfusion and oxygenation dynamics under repeated ischemia–reperfusion cycles (**Fig. 1d**). Results showed significant decreases in perfusion and oxygenation during occlusion, followed by rapid recovery after reperfusion, confirming the functional impact on brain metabolism (**Fig. 1e**). Diffusion maps further showed evolving infarction in the frontal brain at sequential time points after balloon-induced occlusion (**Fig. 1f**). Together, these results establish the micro-balloon as a reliable and repeatable tool for reversible modulation of cerebral blood flow, providing a powerful platform to dissect the early onset and recovery mechanisms of ischemic stroke.
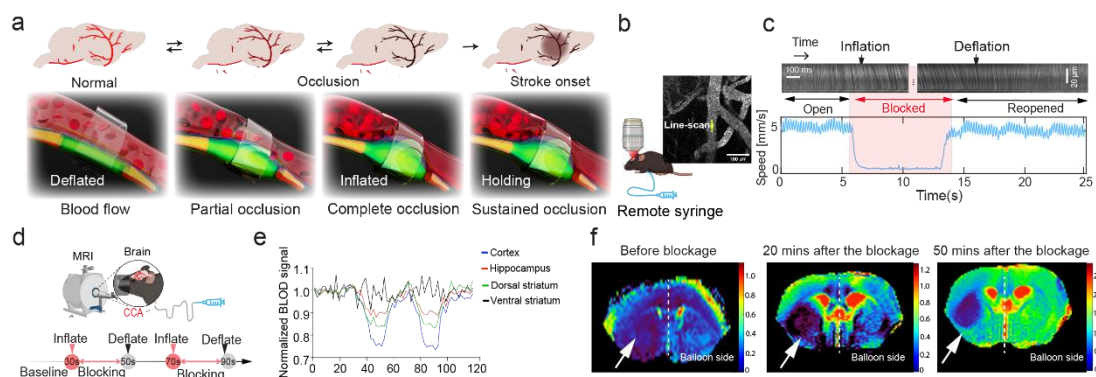

Fig. 1 | Micro-balloon–based reversible ischemia model. (a) Balloon placement and inflation on the CCA. (b-c) Two-photon imaging confirms reversible loss and recovery of capillary velocity. (d-e) Repeated cycles reveal consistent control of perfusion and oxygenation. (f) Diffusion maps of the frontal brain at various time points after micro-balloon–induced infarction (white arrow).

Conclusion

The micro-balloon enables rapid, reversible, and reproducible control of cerebral blood flow in mice, providing a reliable ischemia–reperfusion model. This approach allows precise dissection of stroke onset and recovery dynamics under advanced imaging platforms.

Empirically Informed Blood Vessel Network Reconstruction for Multimodality Image-based Vascular Systems Biology

Yiyang Huang[1*], Reshmi Patel[4*], [1]Akanksha Bhargava[5], and [1]Arvind P Pathak[1, 2, 3]

Dept. of Biomedical Engineering[1], Sidney Kimmel Comprehensive Cancer Center[2], Russell H. Morgan Dept. of Radiology and Radiological Science[3], The Johns Hopkins University School of Medicine, Baltimore; Dept. of Biomedical Engineering, University of Texas Austin[4], Dept. of Biomedical Engineering[5], University of New South Wales, Sydney, Australia,

Background: 3D modeling of cerebral blood flow offers a powerful framework for investigating brain pathologies with high morbidity and mortality in the United States, including neurodegenerative diseases, stroke, and cancer[1]. Such computational models enable the generation of metabolic and hemodynamic predictions within both diseased and surrounding tissue, possible with superior spatial and temporal resolution compared to conventional functional imaging modalities. Although 3D blood flow modeling has been employed in various contexts, its application to high-resolution brain vascular networks remains limited due to the limitations of image derived vessel topology. The vascular topology derived from conventional 3D imaging methods such as MRI, CT or light-sheet microscopy cannot be directly used for blood flow simulations due to inevitable gaps in the vasculature from imaging or contrast labeling artifacts. These gaps may occur in any vessel regardless of radius, which significantly changes the direction and magnitude of the simulated flow, rendering the modeling result physiologically inaccurate. Current methods to fill these gaps usually work on specific vessel networks acquired or imaging modalities[2] and do not consider diseased-induced changes in vascular architecture. **Objective:** To develop a 3D vascular network-filling method that is independent of imaging modality- and spatial resolution and is informed by vascular biology and empirical data. The goal is to restore missing vessels in the vascular network derived from imaging data to enable high-fidelity simulations of blood flow. **Methods:** The algorithm was implemented in MATLAB to perform gap filling in 3D vessel graph data generated from AMIRA software. For each network, candidate connections were identified and classified based on their node degree, with morphological features (e.g. radius and orientation angle) computed and compared to extant feature distributions of the network to assess the likelihood of establishing a connection. To account for tumor-induced vascular remodeling[3] potential connections in brain-tumor associated, networks were extended up to the third-degree nodes, in contrast to the second-degree limit applied to healthy networks. Loose vessel segments unconnected after gap filling were removed, leaving one fully connected network. The algorithm's performance was first evaluated on synthetic vascular trees with controlled volume fractions ranging from 100% to 79%, using percentage overlap and chamfer distance between nodes in vessel network graph. To further assess robustness, the same synthetic datasets were perturbed with simulated noise representative of micro-computed tomography (μCT) imaging artifacts. Finally, the method was applied to experimental datasets, including a μCT-acquired brain tumor-bearing mouse brain ($7\mu m$ isotropic), a magnetic resonance imaging (MRI)-derived healthy mouse brain ($40\mu m$ isotropic), and a light-sheet microscopy (LSM)-imaged mouse hippocampus ($1.6\mu m \times 1.6\mu m \times 1\mu m$). **Results:** For the synthetic datasets, the vascular showed near perfect resemblance to the original network after gap filling when the volume fraction was >92% (**Fig. 1A-B**). The algorithm restored more gaps between 92% and 80% volume fractions, with a drastic decline in gap filling for networks with volume fraction <80%. Noisy segments reduced reconstruction accuracy by diverting focus from true gaps (**Fig. 1C-F**). In de facto datasets acquired from CT, MRI, and LSM, our method reconnected significant missing portions while preserving network features (**Fig. 1G-H, 1J-K, 1M-T**). Comparison between the tumor vasculature network and healthy vasculature network revealed vessel topology and morphology differences, consistent with those reported in the literature (e.g. tumor networks exhibited more trifurcation and elevated vessel diameter[3]), and warranted a separate gap filling method in our algorithm (**Fig 1I-L**). **Conclusions:** Our method showed efficient restoration of full vascular network connectivity derived from common imaging modalities at different imaging resolutions. We also demonstrated the importance of applying different biology-informed rules in reconstruction of healthy and tumor vascular networks.

1. FASTSTATS - leading causes of death [CDC website]. Centers for Disease Control and Prevention. June 26,2025.https://www.cdc.gov/nchs/fastats/leading-causes-of-death.htm Accessed Jul 22 2025.
2. Moccia S, De Momi E, El Hadji S, Mattos LS. Blood vessel segmentation algorithms — review of methods, datasets and Evaluation Metrics. Computer Methods and Programs in Biomedicine. 2018;158:71–91.
3. Less JR, Skalak TC, Sevick EM, Jain RK. Microvascular network architecture in a mammary carcinoma. *Experientia Supplementum*. 1992;74–80.
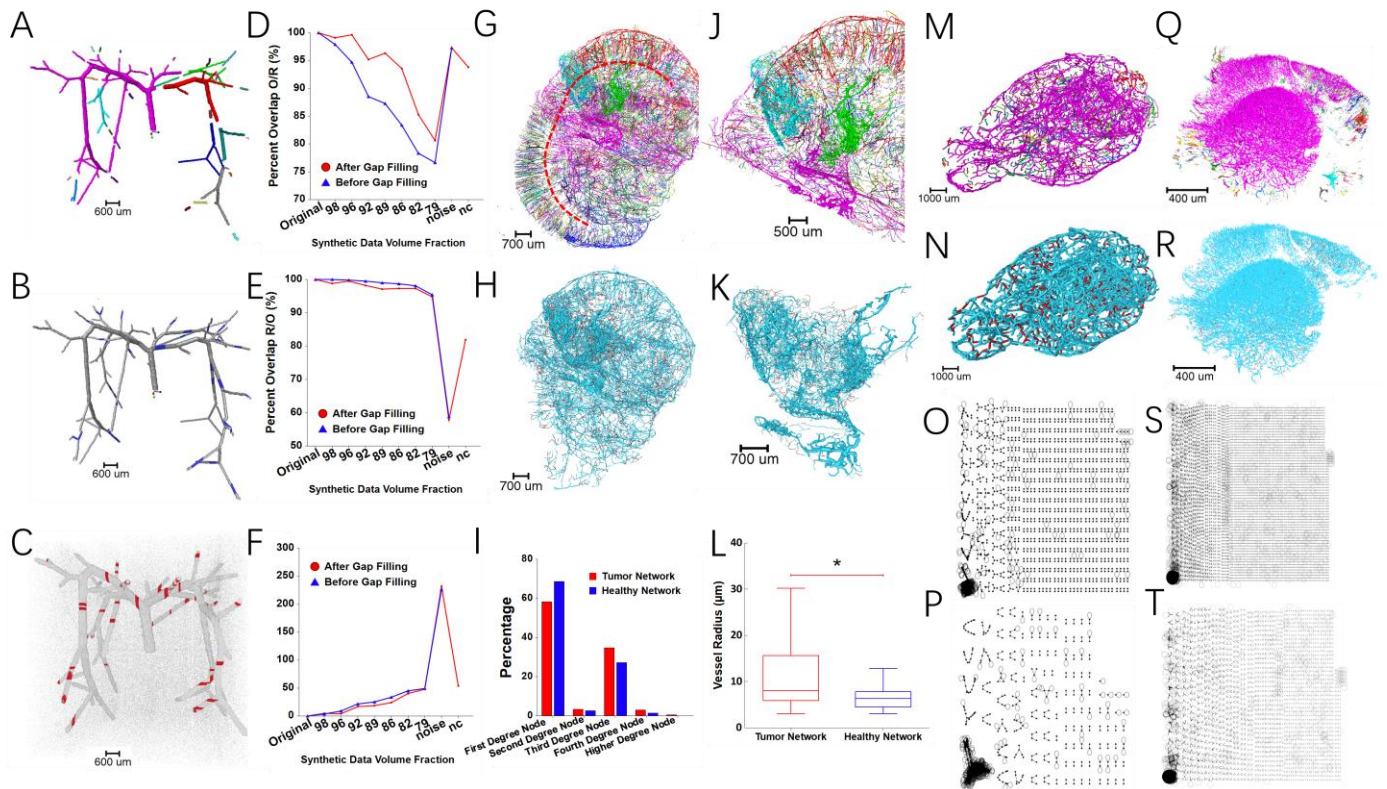
Figure 1. (A) Binarized image volume of the synthetic vascular tree with volume fraction of 96%. Each color represents a connected component. **(B)** Gap filling result of Vascular tree in A). Bridge vessels are shown in blue. **(C)** The same synthetic vascular tree from (A) with noise added (SNR = 2). Deleted vessel segments shown in red. Reconstruction accuracy metrics for the synthetic vascular tree: **(D)** % overlap between the original and reconstructed vascular trees (O/R %overlap), nc represents noise cleaned (after removal of short unconnected vessel segments). **(E)** % overlap between the reconstructed and original vascular trees (R/O %overlap). **(F)** Chamfer distance between vascular tree before and after reconstruction to the gap-free vascular tree. **(G)** Overview of whole brain vasculature and **(J)** brain tumor and surrounding vasculature acquired with μCT. Each color represents a local vessel network not connected to other local network. Red dashed line separates the cortical and subcortical regions of the brain. **(H, K)** Fully connected vascular networks after gap filling and removal of unconnected vessel segments. Cyan represents original vessels and red represents new bridge vessels. **(I)** Degree node distribution in healthy and tumor vascular networks. **(L)** Vessel radius distribution in tumor and healthy mouse brain vascular networks. **(M)** MRI-derived vascular network before gap filling. Each color represents a local vessel network not connected to other local network. **(N)** Fully connected MRI vascular network showing filled gaps in red. Network representation of the MRI-derived vascular network before **(O)** and after **(P)** gap filling. **(Q)** LSM-acquired vascular network before gap filling. Each color represents a local vessel network not connected to other local network. **(R)** Fully connected LSM vascular network showing filled gaps in red. Network representation of LSM vascular network before **(S)** and after **(T)** gap filling.

Mapping of GABA and Glutamate in Tuberous Sclerosis Complex Using Edited-MRSI

Dillip K. Senapati[1], Helge J. Zöllner[1], İpek Özdemir[1], Georg Oeltzschner[1], Ryan Gill[1,2], Jacqueline Harris[1,2], Peter B. Barker[1,2], and Doris D.M. Lin[1,2]

[1]*Department of Radiology, Johns Hopkins University* , [2] *Kennedy Krieger Institute, Baltimore, MD, USA*

Background: Tuberous sclerosis complex (TSC) is a genetic disorder affecting multiple organs, including the brain, and is commonly associated with cognitive deficits and seizures[1]. GABA and glutamate are the major inhibitory and excitatory neurotransmitters in the brain, respectively, and their imbalance has been implicated in epilepsy. Only a limited number of prior studies, mostly single-voxel, have investigated GABA levels in TSC using MR spectroscopy (MRS) [2,3].

Objective: To map GABA and glutamate plus glutamine (Glx) levels in TSC using GABA-edited MRSI, and compare to those in healthy controls (HC).

Methods: <u>*Subjects*</u>: The study was approved by the JHMIRB. 13 subjects with a clinical or genetic diagnosis of TSC[1] (9M/4F, 16.0 ± 8.1, range 5-31 yrs.) and 20 HC Subjects (9M/11F, 20.7 ± 7.3, range 8-32 yrs.) were included in the analysis. <u>*MRI:*</u> All scans were performed on a Philips 3T 'Ingenia Elition' scanner equipped with a 32-channel receive head coil. The MR protocol included anatomical MRI and water and GABA-edited multi-slice MRSI[4]. Three MRSI slices were recorded with a circular k-space sampling, 14x18 matrix, nominal voxel size 12x12x14 mm (≈ 2.2 cm^3). For GABA-edited MRSI, hypergeometric dual-band (HGDB) water and lipid suppression pulses and outer-volume suppression (OVS) was used[5], with scan parameters TR/TE 1.8s/68ms, 4 NEX, edit ON/OFF 1.9/0.7 ppm, scan time 23m 40s. Water MRSI scan parameters were TR/TE 0.85s/20ms, 1 NEX, scan time 2m 48s. <u>*MRSI Reconstruction and Analysis:*</u> MRSI data were reconstructed in 'Osprey'[6], including retrospective motion compensation[7] on raw k-space data followed by coil-combination and phase-correction. Metabolite concentrations were estimated with linear-combination modeling (LCM) using a basis set simulated with MRS Cloud[8], and quantified relative to both total creatine (tCr);from short-TE MRSI and H$_2$O. <u>*Voxel selection & statistical analysis*</u>: ROIs were selected using 'FSLeyes' [9] in lesions and normal-appearing brain regions in white, gray and deep-gray matter, as visualized on FLAIR MRI. Metabolite levels were compared between TSC and HC using ANOVA with post-hoc Bonferroni correction ($\alpha < 0.05$).


Figure 1: **(A)** Example GABA-edited spectra from a 10 y.o. subject with TSC, **(B)** Box plots of GABA+/tCr & Glx/tCr in WM (white matter), GM (gray matter), DG (deep gray) & tubers in TSC and HC, and **(C)** example metabolite maps in 1 TSC and 2 HC subjects.

Results: Example spectra(M/10) are shown in Figure 1A. Both GABA+/tCr and Glx/tCr were significantly increased in TSC compared to HC in white and deep gray matter, as well as tubers (Figure 1B, $p < 0.05$). Water-referenced analyses (not shown) yielded similar results. GABA+/tCr and Glx/tCr maps are shown in Figure 1C.

Conclusions: Edited-MRSI was feasible in subjects with TSC, and indicated diffusely increased levels of both GABA+ and Glx compared to HC. Elevation of GABA in TSC is consistent with prior single voxel studies [10,11], and our own short-TE MRSI study also showed Glx elevation in TSC [12]. Further work is needed to understand the underlying mechanisms for altered GABA and Glx levels, the effects of age and medication, and also the relationship with seizures and cognitive impairment.

References: [1]Northrup, Ped Neurol (2013), [2]Aasly, Epil Rsch(1999), [3]Mori, Brain & Dev (2012), [4]Zhu, MRM (2011), [5]Zhu, MRM (2010), [6]Oeltzschner J Neurosci Methods (2020), [7]Chan, Neuroimage (2019), [8]Hui MRM (2022), [9]McCarthy (2024). FSLeyes (1.11.0), [10] Sarlo, Seizure: European Journal of Epilepsy (2021), [11]Taki, Neuroimage (2009), [12]Senapati et al. (AJNR, *in review*).
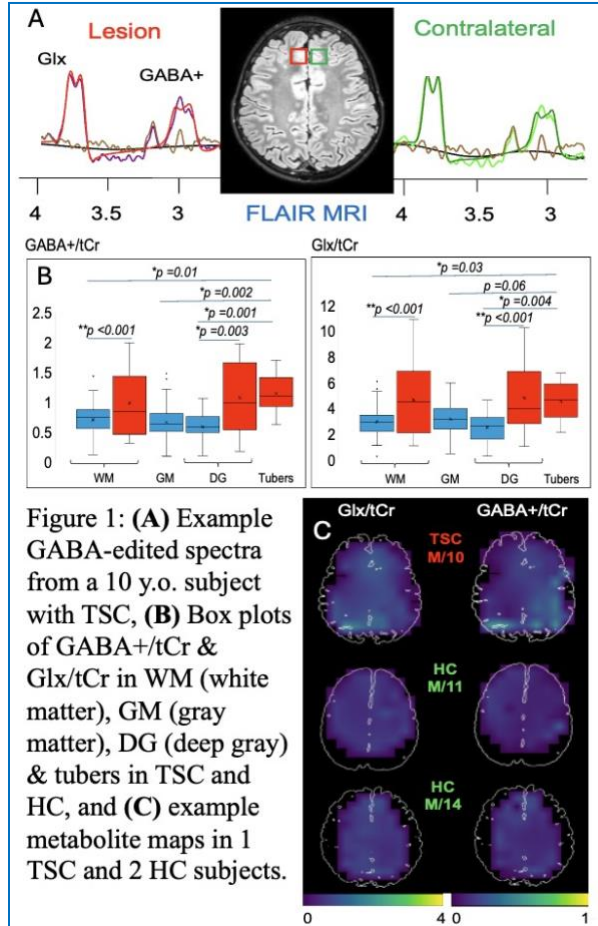
Integrated MRI and Near-Infrared Imaging of Ovarian Cancer
via Folate-Targeted Dual-Mode-Dual-Gd/ICG Liposomes

Bonghwan Chon, PhD[1], Mukesh P. Yadav, PhD[1], Ananth Annapragada, PhD[2], Bahman Anvari, PhD[3], James Bankson, PhD[4], Anil K. Sood, MD[5] and Vikas Kundra, MD, PhD [1,6]*

[1]Department of Diagnostic Radiology and Nuclear Medicine, University of Maryland School of Medicine, Baltimore, MD, USA
[2]Baylor College of Medicine and Texas Children's Hospital, Houston, TX, USA
[3] Department of Bioengineering and Department of Biochemistry, University of California, Riverside, CA, USA
[4]Department of Imaging Physics, The University of Texas MD Anderson Cancer Center, Houston, TX, USA
[5] Department of Gynecologic Oncology and Reproductive Medicine, The University of Texas MD Anderson, Houston, TX, USA
[6]Marlene and Stewart Greenebaum NCI Comprehensive Cancer Center Program in Oncology, Experimental Therapeutics, University of Maryland School of Medicine, Baltimore, MD, USA

Background: Dual-mode-dual-Gd (DMDG-ICG) nanoparticles enable both magnetic resonance (MR) and near-infrared (NIR) optical imaging for enhanced tumor visualization. Liposomes of certain size localize to tumors "passively" via enhanced permeability and retention effect. However, this may limit sensitivity and specificity. There is controversy whether "active" targeting can improve imaging of nanoparticles, and there is a dearth of such studies for dual modality imaging. Folate receptor alpha (FR-α) is overexpressed in a majority of ovarian cancers and represents a potential target for tumor-specific imaging.

Objective: To evaluate whether folate receptor targeting enhances the localization and dual-modality imaging performance of DMDG-ICG liposomes in intraperitoneal ovarian tumor models.

Methods: FR-α expression in SKOV3 and HeyA8 ovarian cancer cells were evaluated by flow cytometry. Three liposomal formulations were prepared: folate-targeted FA-DMDG-ICG, non-targeted DMDG-ICG, and vehicle control. Liposomes were characterized by absorption spectra, NIR fluorescence intensity, T1 relaxivity, and particle size via dynamic light scattering. *In vitro* studies assessed cellular uptake and binding efficiency, including competitive inhibition with excess folate. *In vivo* MRI and NIR fluorescence imaging were performed in SKOV3 tumor-bearing mice to evaluate biodistribution, tumor targeting, and dual-modality imaging performance. *Ex-vivo* analyses were used to confirm *in vivo* imaging findings.

Results: Flow cytometry confirmed high FR-α expression in SKOV3 cells and low expression in HeyA8 cells. Targeted and non-targeted liposomes had similar physicochemical characteristics. *In vitro*, FA-DMDG-ICG showed significantly higher binding and uptake in SKOV3 cells compared to non-targeted liposomes, which was reduced by excess free folate, confirming FR-α–specific targeting. *In vivo*, FA-DMDG-ICG liposomes produced enhanced MR contrast-to-noise ratios and higher NIR fluorescence signals in SKOV3

Figure Representative open abdomen fluorescence images of nude mice bearing SKOV3 IP tumors, captured two days after injection of various imaging agents; FA-DMDG-ICG, DMDG-ICG, FA-DMDG-ICG with free FA, and vehicle. The FL imaging was performed using an excitation (emission) window of 745 ± 15 (820 ± 10 nm) for ICG's FL. The yellow outlines indicate the tumor, and 'L' denotes the liver.

tumors relative to non-targeted liposomes and relative to competitive inhibition with free folate ($p < 0.05$). *Ex vivo* analysis corroborated *in vivo* findings of improved tumor localization with folate-targeted liposomes.
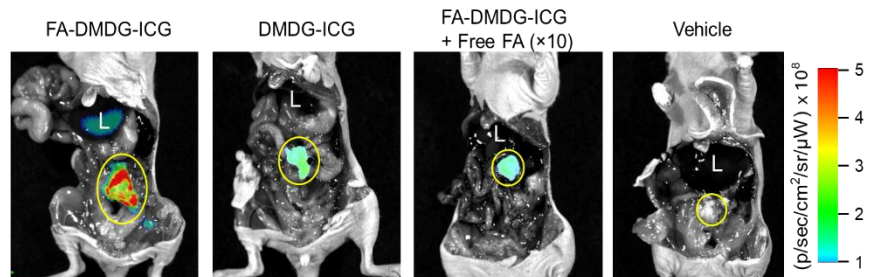
Conclusions: "Active" targeting can improve imaging nanoparticle imaging by two separate modes, MR and NIR, compared to "passive" tumor targeting as demonstrated in an intraperitoneal ovarian tumor model using Folate receptor–targeted FA-DMDG-ICG. Findings suggest potential clinical utility of these nanoparticles for preoperative tumor localization and intraoperative guidance in ovarian cancer surgery.

Bridging Brain Activity and Behavior with Molecular Imaging and Deep Learning

Subhrajit Das[1], Janaka Senarathna[2], Vu Dinh[2], Amit Banerjee[3], Ralph Etienne-Cummings[1] and Arvind P. Pathak[1,2,4]

Depts. of [1]Electrical and Computer Engineering, [2] Radiology and Radiological Science, [3]Applied Physics Laboratory and [4]Biomedical Engineering, Johns Hopkins University, Baltimore, MD 21218.

Introduction: One of the central aims of systems neuroscience is to unravel the complex relationship between neural activity and behavior. Achieving this understanding is not only critical for advancing knowledge of neurological disorders, but also for designing precise, feedback-based therapeutic strategies. A notable example is Deep Brain Stimulation (DBS), which has shown success in treating Central Nervous System (CNS) disorders such as epilepsy and stroke, with recent breakthroughs in Parkinson's disease highlighting the benefits of dynamically adjusting DBS parameters based on behavioral feedback. To enable such adaptive interventions, researchers are actively working to establish reliable mappings between molecular neuroimaging data and behavioral states in preclinical models. Recent advances in miniaturized microscopes, or miniscopes, have made it possible to capture continuous multichannel neuroimaging data (i.e. neural activity, cerebral blood flow (CBF), and cerebral blood volume (CBV)) simultaneously with behavioral recordings of freely moving mice [1]. However, the large (~100 GB) dataset size and behavioral complexity make linking neural activity to behavior challenging. Although traditional image processing and machine learning (ML) approaches have been applied to analyze such molecular neuroimaging data, they often lack accuracy in decoding physiological signals to behavior while demanding extensive computational time. As a result, action-recognition frameworks that exploit Convolutional Neural Networks (CNNs) for extracting spatial features and Recurrent Neural Networks (RNNs) for extracting temporal dynamics are being adopted for predictive modeling. This study evaluates the performance of a CNN-RNN model using neuronal activity images acquired from a miniscope [1]. If successful, real-time behavior prediction with such DL models would: (i) enable high-throughput estimation of "neurophysiology-to-behavior" transfer functions for relevant actions (running, whisking, eating, sleeping, etc.); (ii) have the potential to power closed-loop therapeutics in which deviations of a patient-specific transfer function could trigger adaptive DBS for Parkinsonian symptoms; (iii) accelerate theranostic and drug-discovery workflows via efficacy readouts.

Methods: Using the miniscope shown in **Fig. 1a**, we recorded multichannel neuroimaging data from awake mice by mounting the device onto the skull (**Fig. 1b**). This optical system imaged a 3 mm × 3 mm region of the sensory–motor cortex through a cranial window. **Fig. 1c** shows the neuronal activity and corresponding time-series acquired with the fluorescence (FL) channel of the miniscope over 18 hours. For the FL data, images were resampled from 512×512 to 224×224 pixels using nearest neighbor of 3×3 kernel size. Recordings were acquired from five healthy, freely behaving mice (M1–M5) over 24-hours, synchronized with behavioral videos annotated using Behavior Cloud software. Behavioral "syllables" included Running (*Run*), Nest Building/Eating (*EoNB*), and Minimally Mobile (*Minimob*). Each FL image sequence comprised 12 consecutive frames (~1 min) and was time-locked to the corresponding behavioral label. Due to prolonged inactivity of the mice, datasets were class-imbalanced and dominated by *Minimob* states. For behavior classification, we designed a CNN–RNN pipeline (**Fig. 1d**). Augmentations (flips, random crops, 30°/60° rotations) expanded training diversity. A ResNet50-BiLSTM model extracted spatiotemporal features, with a 20% dropout applied before a fully connected prediction layer. The final 2 layers of ResNet50 along with BiLSTM and fully connected layer were updated during training. Performance was evaluated using 5-fold cross-validation, where in each fold, one mouse was withheld for testing while the remainder of the animals formed the training set. To mitigate class imbalance, *Minimob* and *EoNB* sequences were restricted to ~300 samples to match those in the *Run* class. Cross-validation yielded accuracy, macro-average F1 scores, and confusion matrices, providing a measure of generalizability across animals.

Results, Discussion and Conclusion: Across five leave-one-mouse-out folds, the framework achieved a mean accuracy of **0.85 ± 0.05%** and a mean macro-averaged F1-score of **0.71 ± 0.06**. The confusion matrices revealed that the *Minimob* class was consistently well-classified across folds, while *Run* and *EoNB* exhibited frequent misclassifications. As observed in the confusion matrices in **Fig. 1e**, *Run* was often confused with *EoNB*, and *EoNB* predictions were split between its own class and *Run*. These results emphasize the robustness of the model in detecting the majority behavioral state, while also highlighting challenges in distinguishing minority classes due to class imbalance and inter-animal variability. In summary, this work introduces a novel framework that leverages a single channel of multichannel neuroimaging data (e.g. neuronal/FL) to predict behavioral states of a freely behaving animal and characterizes its potential generalizability.

REFERENCES

1. J. Senarathna, D. Yang, J. Brill, S. Das, S. Bare, Y. Ren, D. VanNess, V. Dinh, I. Karim, A. Banerjee, N. Thakor, M. Ying, and D. Linden, "Cloud-based Functional and Molecular Neuroimaging with Multi-contrast Miniscopes", *Proceedings of the World Molecular Imaging Society,* 2024.
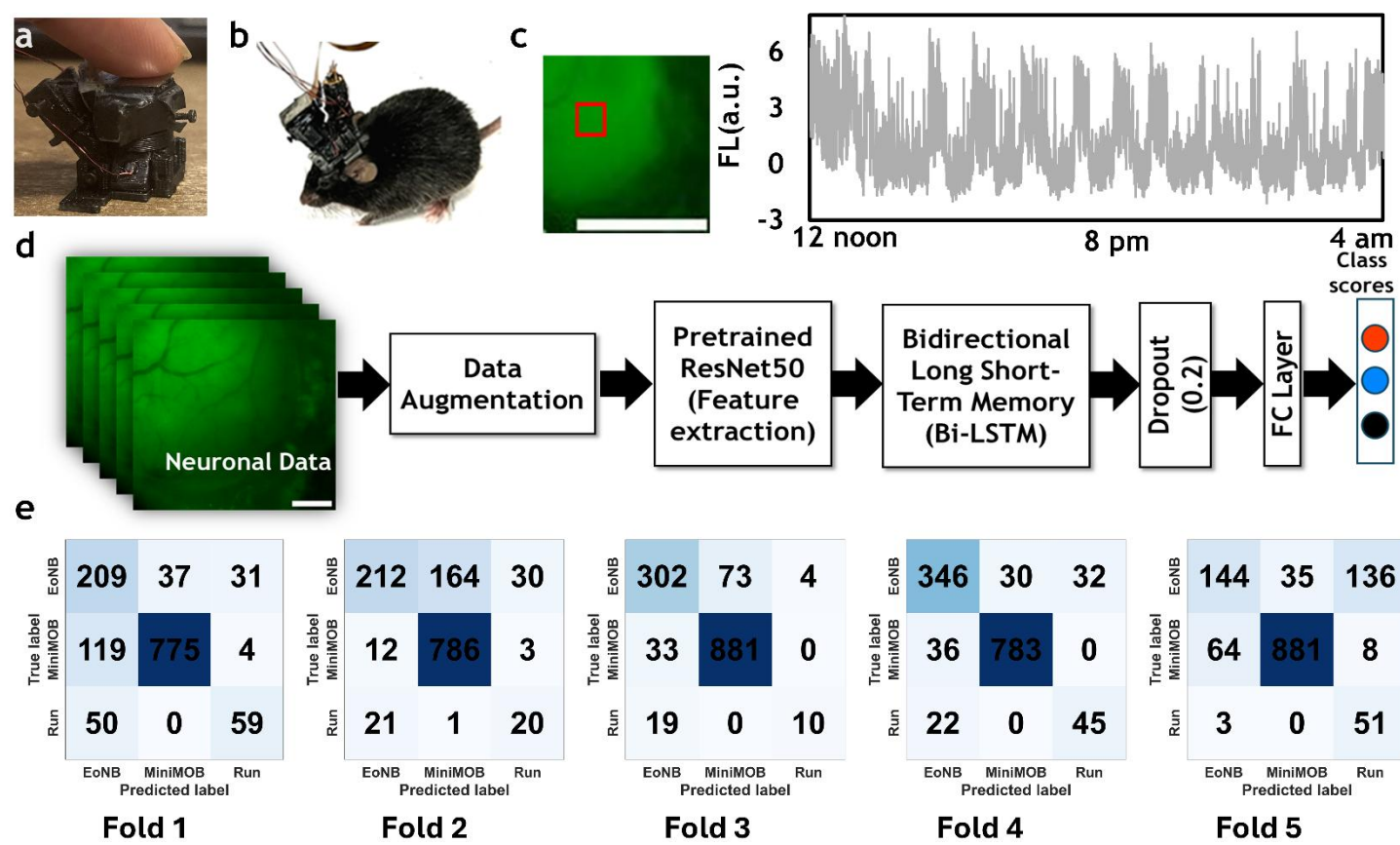
Fig. 1: Bridging Brain Activity and Behavior with Molecular Imaging and Deep Learning. (a) Miniscope capable of multicontrast neuroimaging of a 3 mm × 3 mm region of the sensory-motor cortex. (b) Photograph of a freely moving mouse with the miniscope mounted on its head. (c) A region of interest (ROI) was selected (red square) in the acquired fluorescence (FL) dataset to illustrate the neuronal activity time-series. The scale bar shown here is 0.6 mm. (d) Deep Learning pipeline employed: Data augmentation for the neuronal (i.e. FL) data involved a random combination of vertical flip, horizontal flip, random crop, and rotation of 30° and 60° for each image sequence. We utilized a pre-trained ResNet50-BiLSTM model. To prevent overfitting, a 20% dropout layer was added. Subsequently, a fully connected layer was appended after dropout, to compute class scores for each image sequence. (e) Confusion matrices for behavior classification across six leave-one-mouse-out folds. Each matrix shows the normalized prediction distribution for the three behavioral classes (*Run*, *Minimob*, *EoNB*). While *Minimob* was consistently well-identified across folds, *Run* and *EoNB* exhibited higher misclassification rates, with *Run* often predicted as *EoNB* and vice versa. Values represent the fraction of predictions normalized by the true class.

Image-based "Neurosurveillance" Reveals How Seizures Disrupt the Brain's Microcirculation

Janaka Senarathna, Vu Dinh, Julia Brill, Devorah Vanness, David J. Linden, and Arvind P. Pathak

The Johns Hopkins University School of Medicine

Background: Although many neurological diseases (e.g. Alzheimer's disease, brain cancers etc.) are characterized by disruptions in the brain's microcirculation, it has been challenging to continuously track such microcirculatory changes over hours/days. This is largely due to the limitations of current imaging systems (e.g. MRI/PET) that require animals to be anesthetized during imaging, which also precludes continuous long-term imaging over the duration of the neuropathology being studied.

Objective: To circumvent these limitations and image microcirculatory dysfunction during disease progression, we developed a novel, miniaturized microscope (or miniscope) that is capable of continuously imaging multiple aspects of the cerebral microcirculation over >24 hours in freely behaving mice. We call this capability 'neurosurveillance'.

Methods: The miniscope acquires images at a resolution of 6 µm over a 3×3 mm^2 field of view, and relies on multiple contrast mechanisms. First, it uses the light absorption of erythrocyte-bound oxy- and deoxyhemoglobin to compute maps of cerebral blood volume (CBV) and intravascular oxygen saturation (S_{O2}). Next it uses the orderly flow of erythrocytes inside microvessels detected via laser light to create maps of cerebral blood flow (CBF). It also detects the green fluorescence emitted by GCaMP-bound neuronal Ca^{2+} to create maps of concurrent changes in neuronal activity (Neu_{ACT}). Equipped with the capability to conduct neurosurveillance, we interrogated changes in the brain's microcirculation in a preclinical seizure model.

Results: Traditionally, seizures are considered to be aberrant electrical discharges within the brain. However, we hypothesized that if neurovascular coupling remains intact, the large neuronal activations triggered by a seizure would also result in large increases in CBV, CBF, and S_{O2}. To test this hypothesis, we induced seizures in a cohort of n=4 adult C57BL/6 mice (3F/1M), via an i.p. injection of pentylenetetrazol (PTZ), a GABA$_A$ antagonist. Maps of CBV, CBF, S_{O2}, and corresponding Neu_{ACT} changes were acquired with the miniscope every 5 s over 24 hours through a surgically prepared cranial window over the murine sensorimotor cortex. Seizures were characterized by Neu_{ACT} bursts lasting < 2 mins. Contrary to intact neurovascular coupling, we observed that seizure-induced neuronal hyperactivations were accompanied by brief periods of severe vasoconstriction (i.e. CBV reduction) and drops in CBF. These observations imply that seizures were accompanied by a compromised microcirculatory status for the duration of the seizure. Moreover, the recovery from this compromised status was short-lived, with the cerebrovasculature entering a second phase of severe vasoconstriction and CBF attenuation that was sustained for approximately an hour following seizure termination. Unlike during the seizure, this post-seizure CBV/CBF drop was accompanied by depressed Neu_{ACT} levels and an almost complete lack of animal mobility. CBV/CBF drops did not translate into a consistent drop in S_{O2}, hinting at concomitant metabolic abnormalities. Finally, two out of four animals developed subsequent spontaneous seizures that were similarly characterized by vasoconstriction and hypoperfusion.

Conclusions: Collectively, neurosurveillance enabled us to establish the central role of microcirculatory dysfunction during seizures, and constitutes a novel approach for characterizing the role of the cerebral circulation in health and disease.

An AI-Powered Framework for Super-Resolution Reconstruction of In Vivo Optical Images

[1]Harish Balasubramanian BTech, [2]Arvind P. Pathak PhD, and [2]Janaka Senarathna PhD

Departments of [1]Biomedical Engineering and [2]Radiology and Radiological Science, Johns Hopkins University

Background: *In vivo* optical imaging is the gold standard for probing disease mechanisms at the native scale of individual neurons or microvessels. However, imaging the brain within a living biological system carries inherent challenges that could severely degrade image quality. A low signal-to-noise ratio (SNR) and a limited resolution-speed product are two major drawbacks. Poor SNR stems from the low illumination levels often required to avoid photobleaching[1], while spatial resolution is frequently compromised to promote imaging speed. Collectively, these limitations restrict our capacity to interrogate neurovascular changes that underlie disease progression. Overcoming these hurdles requires learning a complex mapping from noise-ridden, low spatial-resolution images onto their original, high-SNR/resolution counterparts. While numerous artificial intelligence (AI)-based pipelines have been reported for noise suppression and super-resolution reconstruction, a majority of these approaches focus on in vitro or ex vivo images[2]. Traditional AI-approaches also require "hand-crafting" or customizing their loss functions to suit each dataset, thereby restricting generalizability.

Methods: To address this, we utilized an AI architecture called generative adversarial network[3] (GAN). It has two deep learning modules, a generator "G" and a discriminator "D". As shown in **Fig. 1a-c**, "G" generates high-resolution image (RECON, **Fig. 1f**) from its low-resolution, noisy inputs (LR+N, **Fig. 1e**) while "D" learns how to distinguish them from their ground-truths (GT, **Fig. 1d**). The GAN is optimal when "G" produces images indistinguishable from GT. This adversarial approach establishes a generalizable AI without handcrafted features or losses. To test the efficacy of this architecture, we acquired a carefully curated set of high-resolution (~ 6 µm/pixel), high dynamic range (8-bit), wide field-of-view (FoV, 3×3 mm^2) images of microvascular morphology in the murine sensorimotor cortices using light absorption properties of erythrocyte-bound oxy- and deoxy-hemoglobin. Images were acquired via a custom mini-microscope from n=5 freely behaving C57BL/6 mice. To emulate poor SNR, Gaussian noise was added with σ= 1,2…,10 least significant bits, corresponding to up to ~4% of the 8-bit dynamic range. Next, to emulate GPU-based image down-sampling used in fast CMOS image acquisition, we down-sampled images at a spatial scale of 16× in each spatial dimension, corresponding to a 256× reduction in pixel count, using nearest-neighbor interpolation. GANs were trained per animal by using ~13,800 images. Testing was conducted using another ~3400 unseen images from same animal.

Results: **Fig. 1g-h** shows an example, where the average signal intensity of a line region of interest (ROI) placed across a microvessel was monitored over ~4 hours. The high Pearson's correlation coefficient (r=0.99) between GAN-generated (from σ=10 noise and 16× down-sampled images) and ground-truth time series demonstrate our capacity for faithful super-resolution reconstruction. **Fig. 1i** shows the close match between diameters of n=15 microvessels in ground truth (X-axis) and GAN-generated (Y-axis) images from a representative animal. Finally, **Fig. 1j** shows the performance our AI-powered pipeline when input with varying degrees of noise. Performance was quantified using peak-SNR or PSNR[4], a metric of similarity between generated and ground truth images. Even at high noise levels (σ up to 10 with 16× down sampling), PSNR values remained above ~40 dB, which is generally considered excellent in imaging practice.

Conclusion: Our AI-powered framework enables the super-resolution reconstruction of optical images from their noisy, low-resolution in vivo imaging counterparts. Its widespread application could lay the groundwork for accelerating biological discovery by enabling ubiquitous high-resolution in vivo imaging access.

References:
1   Laissue, P. P., Alghamdi, R. A., Tomancak, P., Reynaud, E. G. & Shroff, H. Assessing phototoxicity in live fluorescence imaging. *Nature methods* **14**, 657-661 (2017).
2   Zhang, H. *et al.* High-throughput, high-resolution deep learning microscopy based on registration-free generative adversarial network. *Biomedical optics express* **10**, 1044-1063 (2019).
3   Isola, P., Zhu, J.-Y., Zhou, T. & Efros, A. A, Image-to-image translation with conditional adversarial networks. *Proceedings of the IEEE conference on computer vision and pattern recognition.* 1125-1134 (2017).
4   Alam, M. S. *et al.* Super-resolution enhancement method based on generative adversarial network for integral imaging microscopy. *Sensors* **21**, 2164 (2021).
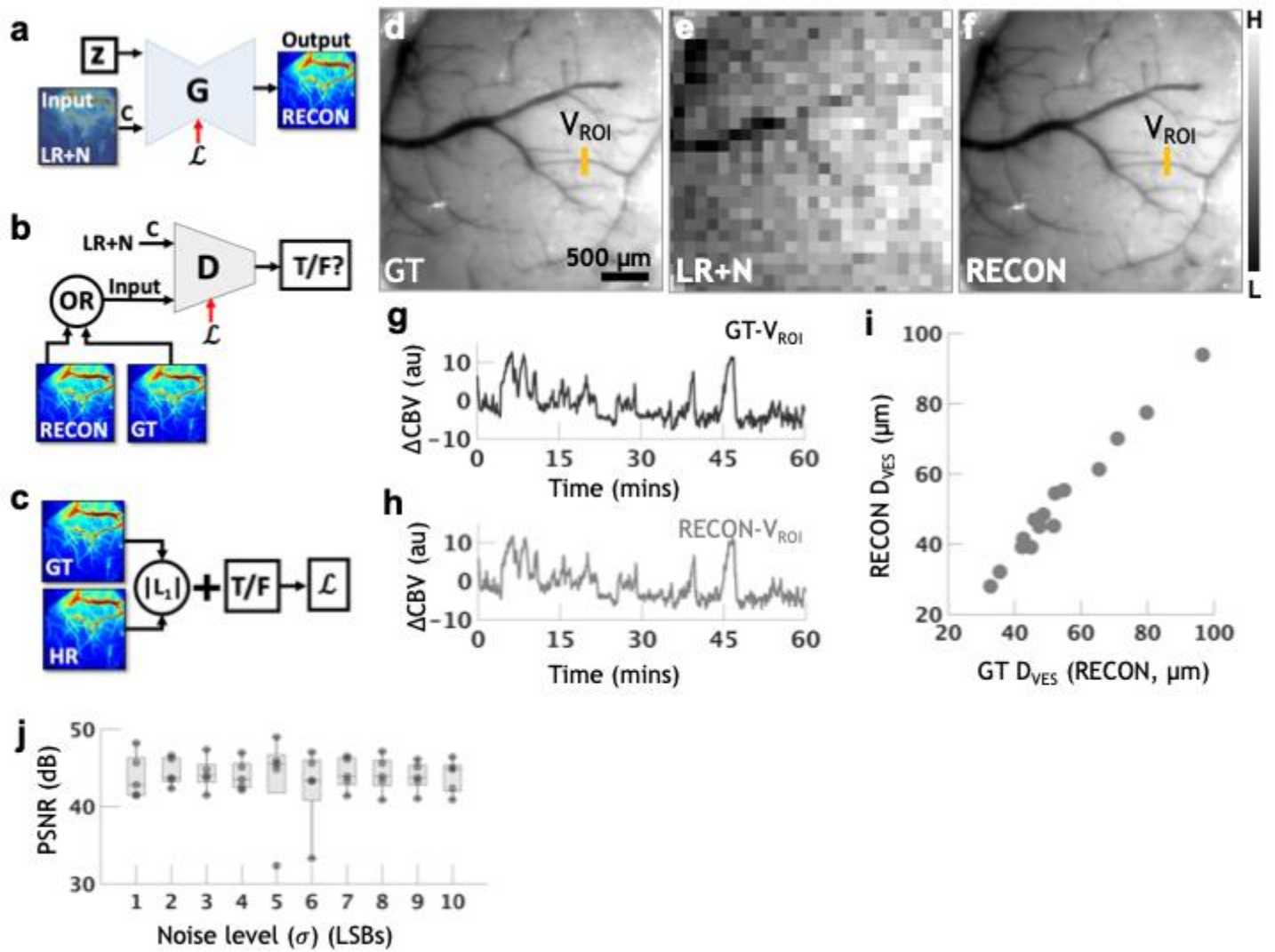
Fig. 1: GAN framework and reconstruction results. (a) Schematic of the generator (G), implemented as a U-Net, reconstructs high-resolution images (RECON) from noisy low-resolution inputs (LR+N). "c" denotes the conditional component of GAN. "z" denotes noise component implemented as dropout during training. **(b)** Schematic of the discriminator (D), implemented as a convolutional neural network to distinguish ground truth (GT) images from RECON images, conditioned on the same LR+N input. **(c)** Training loss comprises an L1 loss between RECON and GT images and an adversarial loss from D. **(d–f)** Representative in vivo images of GT, LR+N and RECON, respectively, showing microvascular morphology within a 3×3 mm^2 field-of-view over the sensorimotor cortex of a mouse. **(g–h)** Time-series showing changes in cerebral blood volume (ΔCBV) extracted from GT (**g**) and RECON (**h**) over 1 hour along a line region-of-interest (ROI), overlaid on a vessel (V$_{ROI}$), marked in d and f. ΔCBV was estimated based hemoglobin light absorption. **(i)** A Scatter plot showing comparison between vessel diameters extracted from GT (x-axis) and RECON (y-axis) for a representative n=15 V$_{ROIS}$ chosen from a single animal. **(j)** Box plots showing peak signal-to-noise ratio (PSNR) between RECON and GT images across n=5 mice. PSNR levels are shown for RECON images generated by using low-resolution (16x down-sampled) inputs degraded with successively higher levels of noise characterized by σ = 1,2, ..., 10 least-significant bits, i.e. up to 4% of the dynamic range of image acquisition. H = high, L=low.

In vivo MPI cytometry of ICV-injected mesenchymal stem cells in a mouse model of Multiple Sclerosis

Kritika Sood, PhD [1,2], Aline Thomas, PhD [1,2], Jeff W.M. Bulte, PhD [1,2], Ali Shakeri-Zadeh, PhD [1,2]

[1]*The Russell H. Morgan Department of Radiology and Radiological Science, Division of MR Research, Baltimore, MD, USA.*
[2]*Cellular Imaging Section and Vascular Biology Program, Institute for Cell Engineering, Baltimore, MD, USA.*

Background: Human mesenchymal stem cells (hMSCs) are a promising therapy for multiple sclerosis (MS) due to their immunomodulatory properties, safety, and low immunogenicity. They can reduce relapse rates, slow disease progression, and promote remyelination. Therapeutic outcomes depend strongly on the delivery route, with intracerebroventricular (ICV) administration offering broad central nervous system (CNS) coverage by leveraging cerebrospinal fluid (CSF) flow and bypassing the blood–brain barrier. To optimize MSC therapies, monitoring biodistribution *in vivo* is crucial. Modalities like MRI provide high-resolution anatomy but lacks sensitivity and quantification. Magnetic particle imaging (MPI), however, enables non-invasive, quantitative, and background-free detection of magnetically labelled cells, allowing longitudinal tracking and refinement of delivery strategies.

Objective: To evaluate the biodistribution and migration of magnetically labelled hMSCs following ICV injection in an experimental autoimmune encephalomyelitis (EAE) mouse model of MS for optimizing cell-based MS therapeutics.

Methods: Fourteen days post-EAE induction, mice (n = 3) received ICV injections of 1.8×10^5 hMSCs labelled with Ferucarbotran (25 μg Fe/mL) and facilitated by poly-L-lysine (3 μg/mL) **(Fig 1.H-I)**. The location of injected cells was monitored over a 7-day period using MPI and computed tomography (CT), enabling *in vivo* quantitative tracking of their localization and migration **(Fig 1. A-D)**.

Results: *In vivo* 2D MPI **(Fig 1. E)** and *ex vivo* MPI confirmed **(Fig. 1D)**, that labelled hMSCs mainly were confined to the brain on Day 1 post-injection with very little off-target presence of signal in peripheral organs such as the liver, which is a limitation often observed with other administration routes. The MPI based cytometry data revealed the stability of the fiducials and the retention of the Ferucarbotran in the brain for 7 days **(Fig 1.F)**. Additionally, *in vivo* 3D MPI/CT imaging revealed the presence of hMSCs within the cerebellum and spinal cord regions on Day 7 post injection **(Fig 1. A-C)** when these cells were absent on Day 1. The presence of labelled hMSCs in these regions was further confirmed in histological analysis of sequential brain sections stained with Prussian Blue and anti-HuNA antibody **(Fig 1. G)**.

Conclusion: The detection of MPI signal in the spinal cord on Day 7, using combined 3D MPI/CT imaging, confirms the presence of labelled hMSCs and their CSF-mediated migration following ICV administration. Histological staining of sequential brain sections further corroborated these findings. These results establish MPI as a powerful, non-invasive, and quantitative tool for *in vivo* cell tracking as well as highlighted its potential to optimize CNS-specific delivery strategies in stem cell-based therapies for MS.
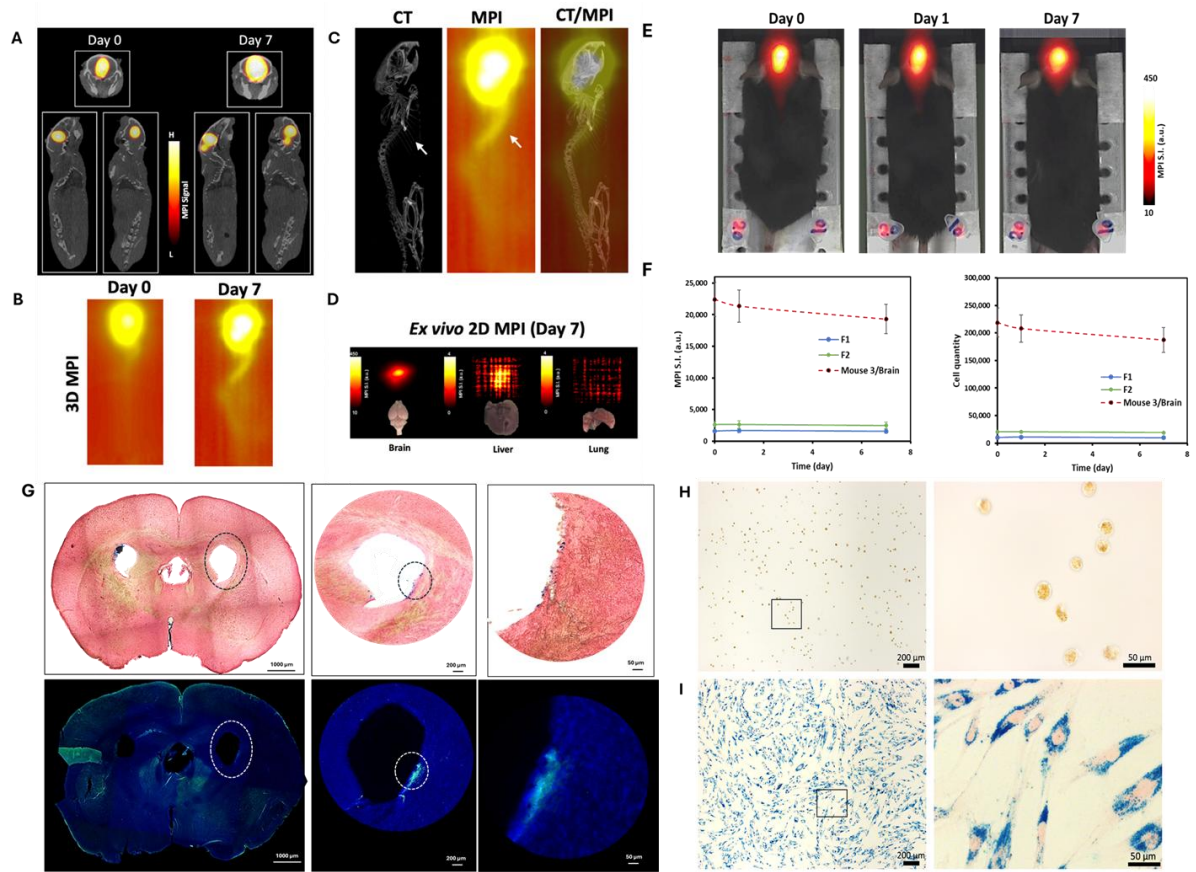
Figure 1: (A) Combination of MPI and CT images to localize the MPI signal within the anatomical context of the mouse brain at Day 0 and Day 7. The signal remains in the brain region with appearance in cerebellum confirming cell distribution over time. (B) 3D MPI images at Day 0 and Day 7 highlighting the spatial distribution of labeled cells within the brain and spinal cord. (C) Merged CT, MPI, and CT/MPI overlay images providing detailed anatomical and functional visualization of labeled cell distribution in the brain and spinal cord regions (See arrows). (D) *Ex vivo* 2D MPI of harvested organs (brain, liver, and lung) at Day 7 confirming strong signal retention in the brain and faint signal in liver. (E) 2D in vivo MPI images at different days post-injection, showing signal localization and intensity in the brain region over time. Signal intensity remains prominent in the brain, gradually decreasing over time, indicating cell retention and potential clearance. (F) MPI signal intensity (left) and corresponding cell quantity (right) over time, showing a significant decline in signal from Day 0 to Day 7, with fiducials containing 10,000 and 20,000 labeled hMSCs (F1 and F2) as stable reference controls for signal quantification. (G) Histological analysis of sequential brain sections from EAE mice on Day 7 post-ICV injection of labeled hMSCs, stained with Prussian Blue and Anti-HuNA, shows the presence of labeled hMSCs within the ventricular region, indicating successful uptake. (H) Labeled hMSCs in a droplet under low and high magnification. (I) hMSCs after Prussian Blue staining, showing labeled cells under low and high magnification. The images confirm successful cell labeling and intracellular uptake of SPIO stained in blue.

Development of Tangle Free Platform for Long-Term Imaging with Head-Mounted Two-Photon Microscope

Baixuan Yang, Jinghui Wang, Honglin Tan, Miroslaw Janowski, Piotr Walczak, Yajie Liang

Department of Diagnostic Radiology and Nuclear Medicine, University of Maryland School of Medicine, Baltimore, Maryland, USA

Background. Head-mounted two-photon microscopy enables high-resolution brain imaging in freely behaving animals, providing insights into brain function during natural behaviors. However, long-term imaging sessions (>1.5 hours) are severely limited by cable entanglement between the head-mounted device and two-photon microscope. As animals rotate and move naturally, the cables twist, ultimately restricting movement and compromising imaging data, beoming a critical barrier for longitudinal neural activity studies involving behavior observations.

Objective. To develop and validate a tangle-free animal imaging platform that enables extended imaging sessions with head-mounted two-photon microscopes.

Methods. We designed a freely rotating cylindrical cage that counterrotates animal rotation **(Fig. 1A, schematic design)**, aiming to prevent entanglement of imaging cables connected to animal head. When an animal rotates, torque is applied to the cable; this force is mechanically converted into counter-rotation of the cylindrical chamber, thereby unwinding cable twists. We characterized the performance of the system by housing mice with the head-mounted miniature two-photon microscope (Mini2P) overnight. Three mice were monitored overnight with head-mounted two-photon microscopes **(Fig. 1B, actual platform setup)**. Videos of animal and platform movements were taken and analyzed by DeepLabCut, deep learning-based pose estimation toolbox, to generate coordinate data which was then computed to reveal animal and container movements using MATLAB. ResNet-101 architecture was trained in DeepLabCut using 12 standard anatomical markers on mouse and 4 container markers respectively **(Fig. 1C)** from representative 12-minute segments of each mouse across multiple recordings.

Results. We first evaluated the performance of DeepLabCut-generated coordinate data by comparing the processed coordinate data against manually labeled ground truth. The automated tracking achieved 98.92% correlation with manually labeled data **(Fig. 1D)**. Next, we plotted the derived net angle changes of mouse and container as well as the total angle changes of mouse, **(Fig. 1E)**, revealing that the container was actively compensating for mouse rotations exceeding 4 turns. Across three mice, the platform kept the net rotation of the mouse within one turn. In the most active subject, the container rotated a total of 4.6 clockwise turns, while the mouse exhibited a residual net rotation of −0.6 counterclockwise turns.

Conclusions. Our findings demonstrated that mice exhibited normal behavioral patterns including exploration, feeding, and rest throughout extended recordings without entangling the device cables. Our tangle-free platform overcomes a fundamental limitation of head-mounted two-photon microscopy, enabling true long-term neural imaging in freely behaving animals. The mechanical counter-rotation system, combined with automated behavioral analysis, provides a reliable solution for extended neuroscience experiments requiring continuous high-resolution brain imaging. This platform opens new possibilities for studying circadian neural dynamics, learning consolidation, and other processes requiring extended observation periods.

References.

Lauer, J., Zhou, M., Ye, S., Menegas, W., Schneider, S., Nath, T., Rahman, M. M., Di Santo, V., Soberanes, D., Feng, G., Murthy, V. N., Lauder, G., Dulac, C., Mathis, M. W., & Mathis, A. (2022). Multi-animal pose estimation, identification and tracking with DeepLabCut. *Nature Methods*, 19(4), 496–504. https://doi.org/10.1038/s41592-022-01443-0

Mathis, A., Mamidanna, P., Cury, K. M., Abe, T., Murthy, V. N., Mathis, M. W., & Bethge, M. (2018). DeepLabCut: markerless pose estimation of user-defined body parts with deep learning. *Nature Neuroscience*, 21(9), 1281–1289. https://doi.org/10.1038/s41593-018-0209-y
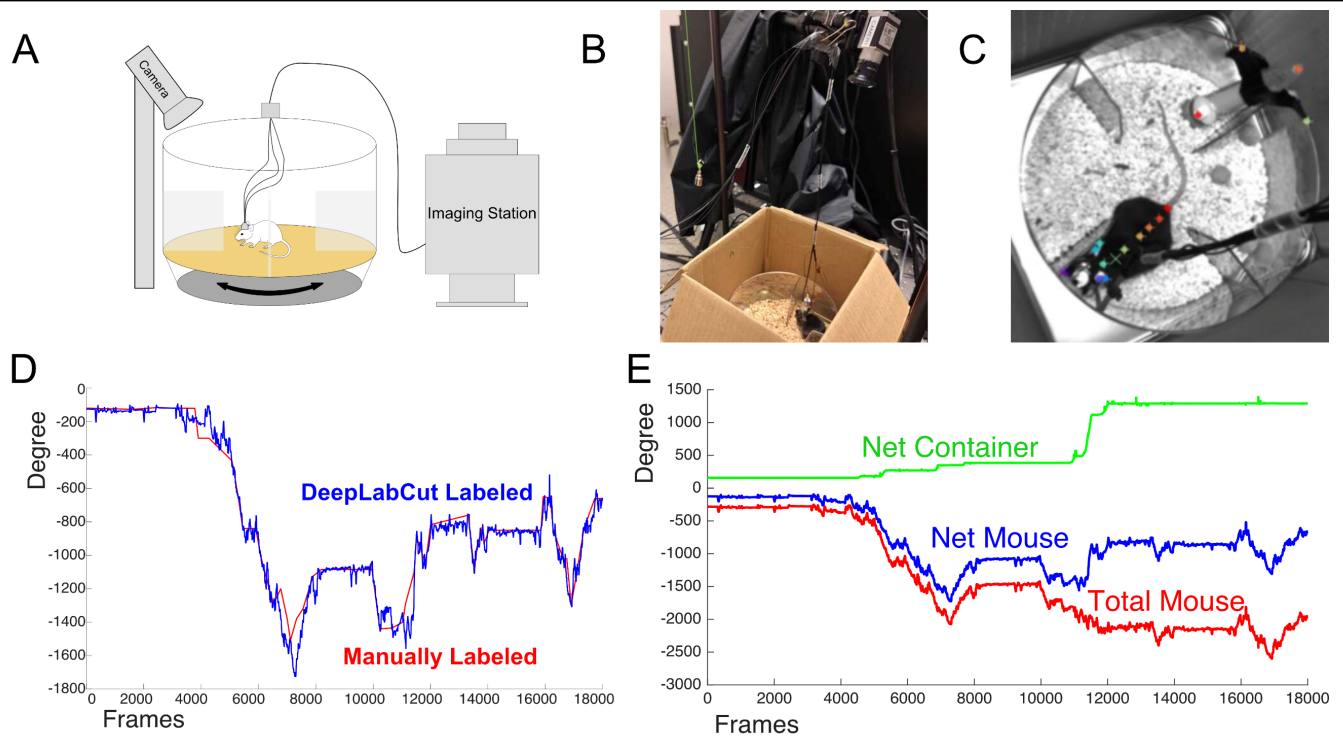
Figure 1. Characterization of tangle-free Mini2P Imaging platform. **(A)** Device setup of freely moving mouse two-photon imaging. **(B)** Positions of platform, mouse, and camera. **(C)** 12 anatomical marks of mouse and 4 markers close to the container edge used in DeepLabCut tracking and angle calculations. **(D)** DeepLabCut tracking performance evaluation (blue) based on manually labeled data (red). **(E)** Comparisons between net container (green) and mouse (blue) angle changes as well as total mouse (red) angle changes, indicating compensation for mouse rotation at certain angle degree.

Rapid Tissue–CSF Water Exchange in the Human Brain Revealed by Magnetization Transfer Indirect Spin Labeling (MISL) MRI

Yihan Wu[1,2], Kexin Wang[1,2], Licheng Ju[1], Jiadi Xu[1,3]

[1] F.M. Kirby Research Center, Kennedy Krieger Research Institute, Baltimore, MD. [2] Department of Biomedical Engineering, Johns Hopkins University, Baltimore, MD. [3] Russell H. Morgan Department of Radiology and Radiological Science, Johns Hopkins University School of Medicine, Baltimore, MD.

**Introduction**: Cerebrospinal fluid (CSF) plays a vital role in protecting and maintaining the brain by regulating its chemical environment, clearing waste, and facilitating nutrient transport[1]. Emerging evidence and imaging technologies have revealed more complex production and circulation pathways, including contributions from ependymal cells and dynamic exchange with interstitial fluid via the glymphatic system[2-5]. Spin-labeling approaches, particularly arterial spin labeling (ASL), have enabled non-invasive detection of CSF production, extending beyond the ventricles to the subarachnoid space[6]. Among newer techniques, Magnetization Transfer Indirect Spin Labeling (MISL) stands out for its high sensitivity to tissue-CSF water exchange[7]. Although promising, MISL has not yet been adapted for human imaging.

**Objective**: In this study, we aim to optimize the MISL technique for human brain applications and establish a quantitative framework for measuring tissue-CSF exchange.

**Methods**: 6 healthy volunteers (age: 24 ± 1 years; 1 female, 5 males) were scanned on a Philips MR Ingenia Elition 3T scanner. As illustrated in the schematic (Figure A), MISL sequence selectively labels the water in brain parenchyma via magnetization transfer (MT), while CSF remains unaffected due to its negligible protein content. Labeled water molecules in the brain parenchyma exchange with CSF, and this exchange can be captured by subtracting the labeled image (acquired at -10 ppm) from the control image (at 200 ppm), producing a difference map indicative of tissue-CSF water exchange. The exchange rate was calculated as $\Delta Z = (S_{control} - S_{label}) / S_{control}$. The MISL
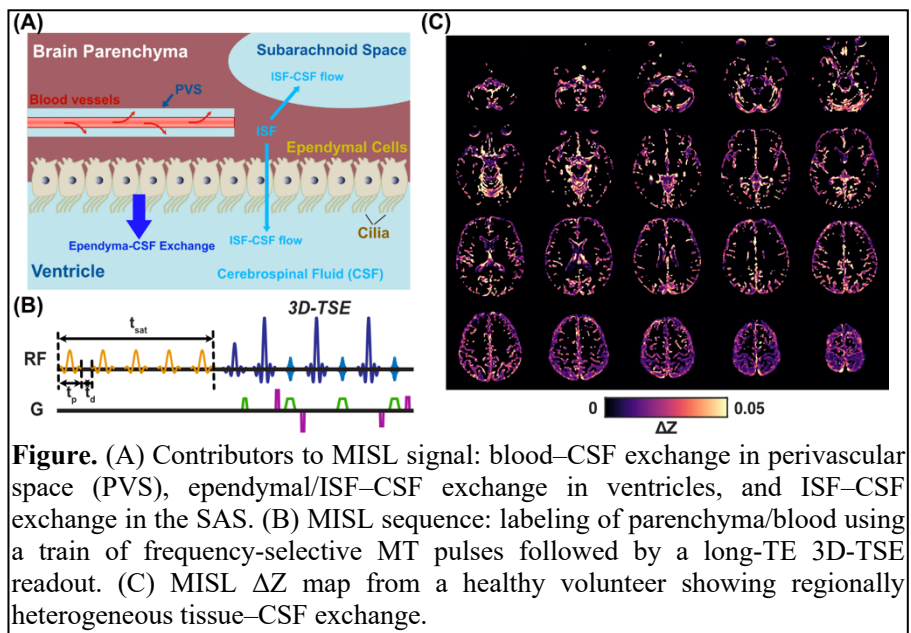

Figure. (A) Contributors to MISL signal: blood–CSF exchange in perivascular space (PVS), ependymal/ISF–CSF exchange in ventricles, and ISF–CSF exchange in the SAS. (B) MISL sequence: labeling of parenchyma/blood using a train of frequency-selective MT pulses followed by a long-TE 3D-TSE readout. (C) MISL ΔZ map from a healthy volunteer showing regionally heterogeneous tissue–CSF exchange.

saturation module (Figure B) consists of a train of frequency-selective MT pulses optimized to maximize labeling efficiency for parenchymal macromolecules while avoiding direct saturation of CSF water. A 3D turbo spin echo (3D-TSE) readout with a long echo time (TE = 1081 ms) was used to suppress background tissue and blood signal, taking advantage of CSF's long T_2 for enhanced contrast. Whole-brain coverage was achieved with a total of 18 dynamic scans, completed in 14.5 minutes.

**Results**: We applied the optimized MISL technique to healthy human participants and successfully visualized in vivo tissue-CSF water exchange across the brain. The MISL ΔZ map (Figure C) demonstrates brain-wide tissue-CSF water exchange, including the choroid plexus, ventricular system, and cerebral and cerebellar subarachnoid space. Notably, significant exchange in the cerebral and cerebellar subarachnoid space suggests that CSF production and turnover are not confined to the choroid plexus alone, supporting the idea of widespread tissue-CSF interaction along the ependymal and subarachnoid surfaces.

**Conclusion**: We successfully optimized and applied the MISL technique for human brain imaging, enabling the quantification of regional tissue-CSF water exchange without the need for exogenous contrast agents. The observed regional variations in tissue-CSF water exchange support emerging models of CSF physiology that incorporate both traditional and alternative circulation pathways, including glymphatic and perivascular contributions. This study establishes MISL as a sensitive and non-invasive method for mapping CSF circulation in the human brain, with promising implications for future research and clinical evaluation of CSF-related neurological disorders.

References:

1. Abate O, Bollo E, Lotti D, Bo S. Cytological, immunocytochemical and biochemical cerebrospinal fluid investigations in selected central nervous system disorders of dogs. Zentralbl Veterinarmed B 1998;45(2):73-85.
2. Iliff JJ, Wang M, Liao Y, Plogg BA, Peng W, Gundersen GA, Benveniste H, Vates GE, Deane R, Goldman SA, Nagelhus EA, Nedergaard M. A paravascular pathway facilitates CSF flow through the brain parenchyma and the clearance of interstitial solutes, including amyloid beta. Sci Transl Med 2012;4(147):147ra111.
3. Iliff JJ, Lee H, Yu M, Feng T, Logan J, Nedergaard M, Benveniste H. Brain-wide pathway for waste clearance captured by contrast-enhanced MRI. J Clin Invest 2013;123(3):1299-1309.
4. Absinta M, Ha SK, Nair G, Sati P, Luciano NJ, Palisoc M, Louveau A, Zaghloul KA, Pittaluga S, Kipnis J, Reich DS. Human and nonhuman primate meninges harbor lymphatic vessels that can be visualized noninvasively by MRI. Elife 2017;6.
5. Ahn JH, Cho H, Kim JH, Kim SH, Ham JS, Park I, Suh SH, Hong SP, Song JH, Hong YK, Jeong Y, Park SH, Koh GY. Meningeal lymphatic vessels at the skull base drain cerebrospinal fluid. Nature 2019;572(7767):62-66.
6. Evans PG, Sokolska M, Alves A, Harrison IF, Ohene Y, Nahavandi P, Ismail O, Miranda E, Lythgoe MF, Thomas DL, Wells JA. Non-Invasive MRI of Blood-Cerebrospinal Fluid Barrier Function. Nat Commun 2020;11(1):2081.
7. Li AM, Chen L, Liu H, Li Y, Duan W, Xu J. Age-dependent cerebrospinal fluid-tissue water exchange detected by magnetization transfer indirect spin labeling MRI. Magn Reson Med 2022;87(5):2287-2298.